



Contents lists available at ScienceDirect

# Journal of the Mechanical Behavior of Biomedical Materials

journal homepage: [www.elsevier.com/locate/jmbbm](http://www.elsevier.com/locate/jmbbm)

## Viscoelastic parameter identification of human brain tissue

S. Budday<sup>a</sup>, G. Sommer<sup>b</sup>, G.A. Holzapfel<sup>b,c</sup>, P. Steinmann<sup>a</sup>, E. Kuhl<sup>d,\*</sup><sup>a</sup> Department of Mechanical Engineering, University of Erlangen-Nuremberg, 91058 Erlangen, Germany<sup>b</sup> Institute of Biomechanics, Graz University of Technology, 8010 Graz, Austria<sup>c</sup> Norwegian University of Science and Technology (NTNU), Faculty of Engineering Science and Technology, 7491 Trondheim, Norway<sup>d</sup> Departments of Mechanical Engineering & Bioengineering, Stanford University, CA 94305, USA

### ARTICLE INFO

#### Keywords:

Human brain  
Rheological testing  
Finite viscoelasticity  
Ogden model  
Parameter identification

### ABSTRACT

Understanding the constitutive behavior of the human brain is critical to interpret the physical environment during neurodevelopment, neurosurgery, and neurodegeneration. A wide variety of constitutive models has been proposed to characterize the brain at different temporal and spatial scales. Yet, their model parameters are typically calibrated with a single loading mode and fail to predict the behavior under arbitrary loading conditions. Here we used a finite viscoelastic Ogden model with six material parameters—an elastic stiffness, two viscoelastic stiffnesses, a nonlinearity parameter, and two viscous time constants—to model the characteristic nonlinearity, conditioning, hysteresis and tension-compression asymmetry of the human brain. We calibrated the model under shear, shear relaxation, compression, compression relaxation, and tension for four different regions of the human brain, the cortex, basal ganglia, corona radiata, and corpus callosum. Strikingly, unconditioned gray matter with 0.36 kPa and white matter with 0.35 kPa were equally stiff, whereas conditioned gray matter with 0.52 kPa was three times stiffer than white matter with 0.18 kPa. While both unconditioned viscous time constants were larger in gray than in white matter, both conditioned constants were smaller. These rheological differences suggest a different porosity between both tissues and explain—at least in part—the ongoing controversy between reported stiffness differences in gray and white matter. Our unconditioned and conditioned parameter sets are readily available for finite element simulations with commercial software packages that feature Ogden type models at finite deformations. As such, our results have direct implications on improving the accuracy of human brain simulations in health and disease.

### 1. Introduction

Understanding the mechanical characteristics of human brain tissue has challenged scientists for many decades. The ultrasound behavior is highly sensitive to spatial and temporal resolutions (McKee et al., 2011). Even for quasi-static loading rates and relatively small strains, brain tissue exhibits a highly nonlinear, hysteretic behavior (Miller and Chinzei, 2002; Franceschini et al., 2006; Budday et al., 2017a), where both time-independent and time-dependent characteristics show regional variations (Jin et al., 2013; Forte et al., 2016; Budday et al., 2017a, 2017b). A key to establish realistic constitutive models for the brain is not only to develop mathematical models that capture the time-dependent tissue response at finite strains but also to design appropriate experiments to accurately identify the corresponding material parameters.

Limited by the availability of human brain tissue (Fallenstein et al., 1969; Galford and McElhaney, 1970; Shuck and Advani, 1972; Donnelly and Medige, 1997; Forte et al., 2016), researchers

alternatively consulted porcine (Miller and Chinzei, 1997; Prange and Margulies, 2002; Rashid et al., 2012) or bovine brains (Bilston et al., 2001; Darvish and Crandall, 2001; Van Dommelen et al., 2010; Budday et al., 2015) due to their structural similarities with the human brain. Animal studies have been exceptionally valuable to better understand the highly complex mechanical response of brain tissue. However, to accurately characterize, model, and simulate the human brain, data from a different species could provide imprecise results (Prange and Margulies, 2002).

Previous studies concerned with the time-dependent mechanical behavior of human brain tissue have mostly been limited to linear viscoelastic properties at small strains (Fallenstein et al., 1969; Galford and McElhaney, 1970; Shuck and Advani, 1972; Donnelly and Medige, 1997; Forte et al., 2016). A popular approach to characterize the time-dependent behavior using a Prony series (Miller and Chinzei, 1997; Prange and Margulies, 2002; Rashid et al., 2012; Budday et al., 2015; Forte et al., 2016), has recently resulted in poor predictions of porcine brain experiments when the actual strain history was taken into account

\* corresponding author.

E-mail address: [ekuhl@stanford.edu](mailto:ekuhl@stanford.edu) (E. Kuhl).<http://dx.doi.org/10.1016/j.jmbbm.2017.07.014>

Received 2 May 2017; Received in revised form 5 July 2017; Accepted 8 July 2017

Available online 11 July 2017

1751-6161/ © 2017 Elsevier Ltd. All rights reserved.

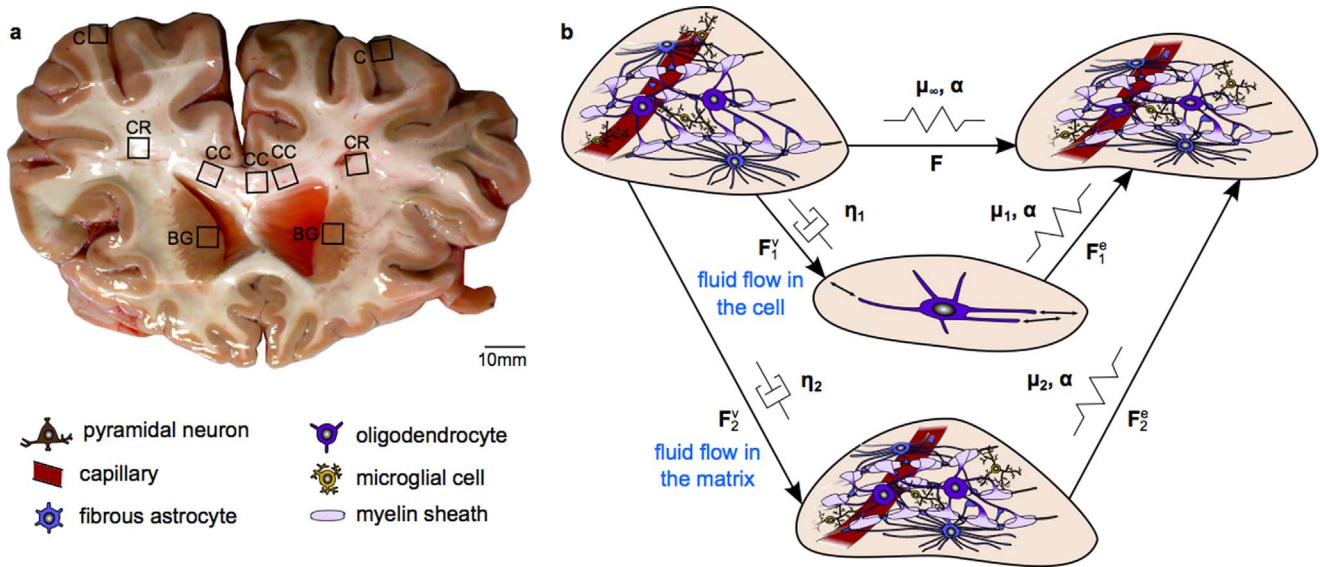


**Fig. 1.** (a) Human brain slice with four characteristic regions, the corpus callosum (CC), the corona radiata (CR), the basal ganglia (BG) and the cortex (C). (b) Multiplicative decomposition model, where  $F$  is associated with the main elastic network characterized by material parameters  $\mu_\infty$  and  $\alpha$ ,  $F_1^e$  is the viscous damper associated with fluid flow inside the cell characterized by the viscosity  $\eta_1$  with the corresponding hyperelastic spring  $F_1^e$  with parameters  $\mu_1$  and  $\alpha$ , and  $F_2^e$  is the viscous damper associated with fluid flow within the solid network of cells and extracellular matrix characterized by the viscosity  $\eta_2$  with the corresponding hyperelastic spring  $F_2^e$  with parameters  $\mu_2$  and  $\alpha$ .

(Labus and Puttlitz, 2016). Since material parameters identified for a single loading mode do not necessarily represent the constitutive behavior under arbitrary loading cases (Miller and Chinzei, 1997, 2002), we are generally limited by the lack of experimental data for accurate parameter identification (de Rooij and Kuhl, 2016). Here, we use the experimental data of human brain tissue under multiple uniaxial loading conditions, cyclic simple shear, unconfined compression, tension, and shear relaxation, and compression relaxation, for four different brain regions, the cortex, the basal ganglia, the corona radiata, and the corpus callosum. To eliminate inter-specimen variations, we performed all five tests sequentially on one and the same specimen. In one region, the corona radiata, we performed additional multiaxial tests (Budday et al., 2017a), combined compression/tension-shear loading, to provide viscoelastic material parameters that are capable of predicting the response of human brain tissue under multiaxial loading conditions. The objective of this study was to systematically compare the viscoelastic response of human brain tissue for five different types of loading and, ultimately, identify a set of material parameters that is best suited to characterize the overall constitutive behavior of four structurally distinct regions of the brain.

We model the finite constitutive behavior of human brain tissue considering a class of viscoelastic models within the general setting of finite deformation continuum mechanics. We multiplicatively decompose the deformation gradient into elastic and inelastic parts (Sidoroff, 1974), and additively decompose the free energy function into equilibrium and non-equilibrium parts (Simo, 1992; Budday et al., 2017b). We introduce internal variables to account for the rate-dependent behavior, and integrate the viscous rate equation in time using an operator split based on an exponential mapping algorithm (Reese and Govindjee, 1998). As the main result of this study, we provide parameter sets for human brain tissue that are directly applicable to finite element simulations in commercial software packages such as Abaqus, where the viscoelastic material behavior is represented through the multiplicative decomposition of the deformation gradient.

An interesting question that has not been fully answered to date is whether different regions in the brain display a different rheology. Regional variations in the characteristic time scales could explain why some studies reported cortical gray matter to be stiffer than white matter (Christ et al., 2010; Budday et al., 2017a), while others found the opposite (Van Dommelen et al., 2010; Budday et al., 2015; Jin et al.,

2013; Weickenmeier et al., 2016). By systematically analyzing time-dependent effects under multiple loading conditions, we carve out possible mechanisms on the cellular level. We emphasize how viscoelastic modeling can implicitly address porous effects caused by the cerebrospinal fluid. The fluid phase makes up about 80% of total brain mass, which is held in the solid network of cells and in the extracellular matrix. To discriminate between the different mechanisms that trigger time-dependent effects, we provide individual parameter sets for the *unconditioned* and *conditioned* tissue response.

## 2. Materials and methods

### 2.1. Experiments

We obtained 1 cm thick coronal brain slices from  $n = 10$  human cadavers ages 54–81, three female and seven male (Budday et al., 2017a). None of the subjects had suffered from any neurological disease known to affect the microstructure of the brain. To minimize tissue degradation, we kept the tissue samples refrigerated at 3°C and humidified with phosphate-buffered saline solution at all times. We completed all tests within less than 60 h post mortem. We extracted specimens of  $5 \times 5 \times 5$  mm from four different regions, the corpus callosum (CC), inner white matter with high fiber density, mostly consisting of uniaxially oriented nerve fiber bundles running between the two hemispheres, the corona radiata (CR), outer white matter with lower fiber density, the basal ganglia (BG), inner gray matter, and the cortex (C), outer gray matter, as illustrated in Fig. 1a. We mounted each specimen onto the triaxial testing device (Budday et al., 2017a) to investigate the mechanical response under multiple loading modes, simple shear, compression, and tension. We conducted all tests at room temperature and chose quasi-static loading conditions with a speed of  $v = 2$  mm/min. In compression and tension, the upper platform of the testing device moved in the  $z$ -direction. In shear, the lower platform moved in the  $x$ - and  $y$ -directions (Sommer et al., 2013). To capture various aspects of the complex response of human brain tissue, we performed two different testing protocols.

The first testing protocol consisted of a sequence of different loading modes as summarized in Table 1. We started with sinusoidal simple shear up to an amount of shear of  $\gamma = 0.2$  in two orthogonal directions, where the amount of shear  $\gamma$  specifies the relative in-plane

**Table 1**  
Testing protocol for sequential shear, compression, and tension.

Protocol: Sequential loading		
•	<b>Simple shear</b> in $x -$ direction three loading cycles	up to $\gamma = 0.2$
•	<b>Stress relaxation</b> in $x -$ direction 300 s holding	at $\gamma = 0.2$
•	<b>Simple shear</b> in $y -$ direction three loading cycles	up to $\gamma = 0.2$
•	<b>Stress relaxation</b> in $y -$ direction 300 s holding	at $\gamma = 0.2$
•	<b>Unconfined compression</b> in $z -$ direction three loading cycles	up to $\lambda = 0.9$
•	<b>Stress relaxation</b> in $z -$ direction 300 s holding	at $\lambda = 0.9$
•	<b>Uniaxial tension</b> in $z -$ direction three loading cycles	up to $\lambda = 1.1$

displacement of two parallel layers in the material body divided by their separation distance. At each recorded time instant, we calculated the shear stresses  $\tau_{xz/yz} = P_{xz/yz} = f/A$  as the shear force  $f$ , the force recorded in the direction of shear, divided by the shear area  $A = WL$  with specimen length  $L$  and specimen width  $W$ . Next, we conducted an unconfined uniaxial compression test up to a compressive stretch of 0.9, a relaxation test of 300 s holding at this compression level, and a uniaxial extension test up to a tensile stretch of 1.1. Hereby, we computed the stretch  $\lambda = 1 + \Delta z/H$  with specimen height  $H$  and  $z$ -displacement  $\Delta z$  and the first Piola stress  $P_{zz}$  as the force  $f_z$  divided by the cross-sectional area  $A$  of the specimen in the unloaded reference configuration, i.e.  $P_{zz} = f_z/A$ . For all loading modes, we applied three loading cycles. We interpreted the first cycle as the *unconditioned* response and the third cycle as the *conditioned* response. For data analysis, we only included specimens, which stayed intact throughout the entire testing protocol in Table 1. If a specimen broke during the course of the protocol, we excluded it from the study. This allowed us to ensure that the obtained material parameters represented the behavior of the same tissue sample under multiple loading modes. Motivated by our previous studies, in which the response of brain tissue was independent of the loading direction (Budday et al., 2017a), we only evaluated the shear data of one direction, the  $y$ -direction. We included data from a total of  $n = 58$  samples:  $n = 13$  from the cortex,  $n = 15$  from the basal ganglia,  $n = 19$  from the corona radiata, and  $n = 11$  from the corpus callosum.

The second protocol consisted of combined compression/tension and shear loading as summarized in Table 2. We first decreased the compressive stretch from 1.00 to 0.75 in increments of 0.05, and subsequently increased the tensile stretch from 1.00 to 1.25, again in increments of 0.05. At each stretch level, we applied three cycles of sinusoidal simple shear up to  $\gamma = 0.2$  in two orthogonal directions. We performed tests according to Protocol 2 data for  $n = 4$  samples from the corona radiata as the other regions did not provide enough space to extract additional reasonably sized specimens after completing Protocol 1.

## 2.2. Kinematics

To characterize the deformation during testing, we use the

**Table 2**  
Testing protocol for combined compression/tension and shear.

Protocol 2: Combined loading	
•	<b>Unconfined compression</b> in $z$ -direction decreasing from $\lambda = 1.00$ to $\lambda = 0.75$ in increments of 0.05 with <b>superposed simple shear</b> in $x$ - and $y$ -direction up to $\gamma = 0.2$ with three loading cycles per direction
•	<b>Uniaxial tension</b> in $z$ -direction increasing from $\lambda = 1.00$ to $\lambda = 1.25$ in increments of 0.05 with <b>superposed simple shear</b> in $x$ - and $y$ -direction up to $\gamma = 0.2$ with three loading cycles per direction

nonlinear equations of continuum mechanics and introduce the deformation  $\boldsymbol{\varphi}(\mathbf{X}, t)$ , which maps the specimen from the undeformed, unloaded configuration with position vectors  $\mathbf{X}$  at time  $t_0$  to the deformed, loaded configuration with position vectors  $\mathbf{x} = \boldsymbol{\varphi}(\mathbf{X}, t)$  at time  $t$ . We determine the associated deformation gradient  $\mathbf{F}$  in its spectral representation in terms of the eigenvalues  $\lambda_a$  and the deformed and undeformed eigenvectors  $\mathbf{n}_a = \mathbf{F} \cdot \mathbf{N}_a$  and  $\mathbf{N}_a$ ,

$$\mathbf{F} = \nabla_{\mathbf{X}} \boldsymbol{\varphi} = \sum_{a=1}^3 \lambda_a \mathbf{n}_a \otimes \mathbf{N}_a. \quad (1)$$

Tables 1 and 2 summarize our testing protocols under simple shear, uniaxial compression and tension, and combined compression/tension and shear. Guided by our experience with adipose tissue (Sommer et al., 2013) and myocardial tissue (Sommer et al., 2015), we assume that our brain samples deform isochorically,  $J = \det(\mathbf{F}) = \lambda_1 \lambda_2 \lambda_3 = 1$ , and homogeneously (Budday et al., 2017a). This implies that we neglect boundary effects and assume a constant deformation gradient  $\mathbf{F}$  across the sample (Rashid et al., 2013). We thus assume the following deformation gradient  $\mathbf{F}$  for simple shear in the  $y$ -direction,

$$[\mathbf{F}]_s = \begin{bmatrix} 1 & 0 & 0 \\ 0 & 1 & \gamma \\ 0 & 0 & 1 \end{bmatrix}, \quad (2)$$

for compression and tension in the  $z$ -direction,

$$[\mathbf{F}]_{c,t} = \begin{bmatrix} 1/\sqrt{\lambda} & 0 & 0 \\ 0 & 1/\sqrt{\lambda} & 0 \\ 0 & 0 & \lambda \end{bmatrix}, \quad (3)$$

and for combined loading,

$$[\mathbf{F}]_{c,t-s} = \begin{bmatrix} 1/\sqrt{\lambda} & 0 & \lambda\gamma \\ 0 & 1/\sqrt{\lambda} & 0 \\ 0 & 0 & \lambda \end{bmatrix}. \quad (4)$$

To model the viscoelastic nature of brain tissue, we decompose the deformation gradient into elastic and viscous parts,

$$\mathbf{F} = \mathbf{F}_i^e \cdot \mathbf{F}_i^v \quad \forall \quad i = 1, \dots, m, \quad (5)$$

where  $i$  denotes the parallel arrangement of  $m$  viscoelastic elements (Sidoroff, 1974). We can then introduce the spatial velocity gradient,

$$\mathbf{l} = \nabla_{\mathbf{x}} \mathbf{v} = \dot{\mathbf{F}} \cdot \mathbf{F}^{-1} = \mathbf{l}_i^e + \mathbf{l}_i^v, \quad (6)$$

and decompose it additively into elastic parts,  $\mathbf{l}_i^e = \dot{\mathbf{F}}^e \cdot (\mathbf{F}_i^e)^{-1}$ , and viscous parts,  $\mathbf{l}_i^v = \mathbf{F}_i^e \cdot \dot{\mathbf{F}}_i^v \cdot (\mathbf{F}_i^v)^{-1} \cdot (\mathbf{F}_i^e)^{-1}$ . From the deformation gradient, we determine the left Cauchy Green deformation tensor  $\mathbf{b}$  and its spectral representation in terms of the principal stretches  $\lambda_a$  and the deformed eigenvectors  $\mathbf{n}_a$ ,

$$\mathbf{b} = \mathbf{F} \cdot \mathbf{F}^t = \sum_{a=1}^3 \lambda_a^2 \mathbf{n}_a \otimes \mathbf{n}_a. \quad (7)$$

It proves convenient, to introduce the elastic left Cauchy Green deformation tensor for each mode,

$$\mathbf{b}_i^e = \mathbf{F}_i^e \cdot (\mathbf{F}_i^e)^t = \sum_{a=1}^3 [\lambda_{i,a}^e]^2 \mathbf{n}_{i,a}^e \otimes \mathbf{n}_{i,a}^e, \quad (8)$$

with eigenvalues  $\lambda_{i,a}^e$  and eigenvectors  $\mathbf{n}_{i,a}^e$ , which are, in general, not identical to the eigenvectors of the total left Cauchy Green deformation tensor,  $\mathbf{n}_{i,a}^e \neq \mathbf{n}_a$ . The material time derivative of the elastic left Cauchy Green deformation tensor,

$$\dot{\mathbf{b}}_i^e = 2 [\mathbf{l}_i^e \cdot \mathbf{b}_i^e]^{\text{sym}} = 2 [\mathbf{l} \cdot \mathbf{b}_i^e]^{\text{sym}} - 2 [\mathbf{l}_i^v \cdot \mathbf{b}_i^e]^{\text{sym}}, \quad (9)$$

introduces the Lie-derivative,

$$\mathcal{L}_v \mathbf{b}_i^e = -2 [\mathbf{l}_i^v \cdot \mathbf{b}_i^e]^{\text{sym}}, \quad (10)$$

along the velocity field of the material motion.

### 2.3. Constitutive modeling

In a previous study, we have shown that, for the current test setup, the constitutive behavior of brain tissue was independent of the loading direction (Budday et al., 2017a). Motivated by these findings, we assume an isotropic material response for both the elastic and the viscoelastic behavior. We introduce the viscoelastic free energy function  $\psi$  as the sum of three terms, an equilibrium part  $\psi^{\text{eq}}$  in terms of the total principal stretches  $\lambda_a$ , a non-equilibrium part  $\psi^{\text{neq}} = \sum_{i=1}^m \psi_i$  in terms of the  $i, \dots, m$  elastic principal stretches  $\lambda_{ia}^e$ , and a term  $p [J - 1]$  that enforces the incompressibility constraint,  $J - 1 = 0$ , via the Lagrange multiplier  $p$ ,

$$\psi = \psi^{\text{eq}} + \psi^{\text{neq}} - p [J - 1] \quad \text{with} \quad \psi^{\text{neq}} = \sum_{i=1}^m \psi_i. \quad (11)$$

Similarly, we introduce the stress power  $\mathcal{P}$  as the sum of an equilibrium part  $\mathcal{P}^{\text{eq}} = \boldsymbol{\tau}^{\text{eq}} : \mathbf{l}$  in terms of the equilibrium Kirchhoff stress  $\boldsymbol{\tau}^{\text{eq}}$  and a non-equilibrium part  $\mathcal{P}^{\text{neq}} = \boldsymbol{\tau}^{\text{neq}} : \mathbf{l}$  in terms of the non-equilibrium Kirchhoff stress  $\boldsymbol{\tau}^{\text{neq}} = \sum_{i=1}^m \boldsymbol{\tau}_i$ ,

$$\mathcal{P} = \mathcal{P}^{\text{eq}} + \mathcal{P}^{\text{neq}} = [\boldsymbol{\tau}^{\text{eq}} + \boldsymbol{\tau}^{\text{neq}}] : \mathbf{l} \quad \text{with} \quad \boldsymbol{\tau}^{\text{neq}} = \sum_{i=1}^m \boldsymbol{\tau}_i. \quad (12)$$

We can then evaluate the dissipation inequality,  $\mathcal{D} = \mathcal{P} - \dot{\psi} \geq 0$ , in terms of the individual equilibrium and non-equilibrium contributions,

$$\mathcal{D} = [\mathcal{P}^{\text{eq}} + \mathcal{P}^{\text{neq}}] - [\dot{\psi}^{\text{eq}} + \dot{\psi}^{\text{neq}}] \geq 0. \quad (13)$$

With the assumption of isotropy, we can rewrite the non-equilibrium stress power in terms of the Lie derivative of the elastic left Cauchy Green deformation tensor (10),  $\mathcal{P}^{\text{neq}} = \sum_{i=1}^m [\boldsymbol{\tau}_i \cdot (\mathbf{b}_i^e)^{-1}] : \frac{1}{2} [\mathbf{b}^e - \mathcal{L}_v \mathbf{b}_i^e]$ , and obtain the following explicit representation of the dissipation inequality,

$$\begin{aligned} \mathcal{D} = & \left[ \boldsymbol{\tau}^{\text{eq}} - 2 \frac{\partial \psi^{\text{eq}}}{\partial \mathbf{b}} \cdot \mathbf{b} \right] : \mathbf{l} \\ & + \sum_{i=1}^m \left[ \frac{1}{2} \boldsymbol{\tau}_i \cdot (\mathbf{b}_i^e)^{-1} - \frac{\partial \psi_i}{\partial \mathbf{b}_i^e} \right] : \mathbf{b}_i^e \\ & - \sum_{i=1}^m \left[ \frac{1}{2} \boldsymbol{\tau}_i \cdot (\mathbf{b}_i^e)^{-1} \right] : \mathcal{L}_v \mathbf{b}_i^e \geq 0. \end{aligned} \quad (14)$$

Following standard arguments of thermodynamics, we obtain the definition of the equilibrium Kirchhoff stress,

$$\boldsymbol{\tau}^{\text{eq}} = 2 \frac{\partial \psi^{\text{eq}}}{\partial \mathbf{b}} \cdot \mathbf{b} = \sum_{a=1}^3 \frac{\partial \psi^{\text{eq}}}{\partial \lambda_a} \lambda_a \mathbf{n}_a \otimes \mathbf{n}_a, \quad (15)$$

the definition of the non-equilibrium Kirchhoff stresses,

$$\boldsymbol{\tau}_i = 2 \frac{\partial \psi_i}{\partial \mathbf{b}_i^e} \cdot \mathbf{b}_i^e = \sum_{a=1}^3 \frac{\partial \psi_i}{\partial \lambda_{ia}^e} \lambda_{ia}^e \mathbf{n}_{ia}^e \otimes \mathbf{n}_{ia}^e, \quad (16)$$

and the reduced dissipation inequalities for each individual mode  $i$ ,

$$\mathcal{D}_i^{\text{red}} = -\boldsymbol{\tau}_i : \frac{1}{2} [\mathcal{L}_v \mathbf{b}_i^e \cdot (\mathbf{b}_i^e)^{-1}] \geq 0. \quad (17)$$

It remains to specify the equilibrium and non-equilibrium parts of the free energy,  $\psi^{\text{eq}}$  and  $\psi^{\text{neq}}$ , and the evolution of the internal variables  $\mathbf{b}_i^e$ . For the equilibrium energy, we follow the recommendations of recent studies that have compared different constitutive models (Budday et al., 2017a; Mihai et al., 2015, 2017) and have identified the one-term Ogden model (Ogden, 1972) to best represent the hyperelastic behavior of human brain tissue,

$$\psi^{\text{eq}} = \frac{2\mu_\infty}{\alpha_\infty^2} [\lambda_1^{\alpha_\infty} + \lambda_2^{\alpha_\infty} + \lambda_3^{\alpha_\infty} - 3], \quad (18)$$

which introduces two parameters, the shear modulus  $\mu_\infty$  and the tension-compression asymmetry parameter  $\alpha_\infty$  (Budday et al., 2017a), and

is parameterized in terms of the total stretches  $\lambda_a$ . The derivative in Eq. (15) then becomes

$$\frac{\partial \psi^{\text{eq}}}{\partial \lambda_a} = 2\mu_\infty \frac{\lambda_a^{\alpha_\infty - 1}}{\alpha_\infty}. \quad (19)$$

For the non-equilibrium energy, we adopt the same Ogden strain energy function (Budday et al., 2017b),

$$\psi_i(\tilde{\lambda}_{ia}^e) = \frac{2\mu_i}{\alpha_i^2} [(\tilde{\lambda}_{i1}^e)^{\alpha_i} + (\tilde{\lambda}_{i2}^e)^{\alpha_i} + (\tilde{\lambda}_{i3}^e)^{\alpha_i} - 3], \quad (20)$$

which introduces two additional parameters  $\mu_i$  and  $\alpha_i$  for each mode  $i$ , and is now parameterized in terms of the deviatoric elastic principal stretches  $\tilde{\lambda}_i^e = (J_i^e)^{-1/3} \lambda_i^e$ , the square roots of the eigenvalues of the isochoric part of the elastic left Cauchy Green tensor,  $\tilde{\mathbf{b}}_i^e = (J_i^e)^{-2/3} \mathbf{b}_i^e$ . The derivatives in Eq. (16) then become

$$\frac{\partial \psi_i}{\partial \lambda_{ia}^e} \lambda_{ia}^e = \frac{2\mu_i}{\alpha_i} \left[ \frac{2}{3} (\tilde{\lambda}_{ia}^e)^{\alpha_i} - \frac{1}{3} (\tilde{\lambda}_{ib}^e)^{\alpha_i} - \frac{1}{3} (\tilde{\lambda}_{ic}^e)^{\alpha_i} \right], \quad (21)$$

where  $a, b, c = \{1, 2, 3\}$  and  $a \neq b, a \neq c$ , and  $b \neq c$ . To a priori satisfy the reduced dissipation inequality (17), we choose the following evolution equation for the internal variables  $\mathbf{b}_i^e$ ,

$$-\mathcal{L}_v \mathbf{b}_i^e \cdot (\mathbf{b}_i^e)^{-1} = \frac{1}{\eta_i} \boldsymbol{\tau}_i, \quad (22)$$

which introduces one additional parameter for each mode  $i$ , the viscosity  $\eta_i > 0$ , or, when scaled with the corresponding shear modulus  $\mu_i$ , the associated relaxation time,  $\tau_i = \eta_i / \mu_i$  (Budday et al., 2017b). Motivated by finite elastoplasticity (Weber and Anand, 1990; Simo, 1992), this choice introduces a dissipation inequality of quadratic form,  $\mathcal{D}_i^{\text{red}} = 1/\eta_i \boldsymbol{\tau}_i : \boldsymbol{\tau}_i \geq 0$ . Since the internal variables  $\mathbf{b}_i^e$  are a linear function of the deviatoric Kirchhoff stress  $\boldsymbol{\tau}_i$ , the elastic deformation always remains volume preserving,  $J_i^e = 1$ , and thus  $J_i^v = J/J_i^e = 1$ . Finally, for comparison with the experimental measurements, we calculate the Piola stress  $\mathbf{P}$  as the partial pull back of the Kirchhoff stress  $\boldsymbol{\tau}$ ,

$$\mathbf{P} = \boldsymbol{\tau} \cdot \mathbf{F}^{-1} = [\boldsymbol{\tau}^{\text{eq}} + \boldsymbol{\tau}^{\text{neq}} - p \mathbf{I}] \cdot \mathbf{F}^{-1}. \quad (23)$$

In unconfined compression and tension, the Lagrange multiplier  $p$  follows from the lateral boundary conditions,  $P_{xx} = P_{yy} = 0$ . In simple shear and combined loading, the shear stresses  $P_{xz}$  and  $P_{yz}$  are independent of the Lagrange multiplier  $p$ . To advance the non-equilibrium part of the constitutive equations in time, we perform an implicit time integration with exponential update (Reese and Govindjee, 1998; Budday et al., 2017b).

### 2.4. Parameter identification

In general, our viscoelastic model has  $2 + 2m + m$  parameters,  $\mu_\infty$  and  $\alpha_\infty$  to characterize the equilibrium response,  $\mu_i$  and  $\alpha_i$  to characterize the non-equilibrium response, and  $\eta_i$  to characterize the relaxation time for each viscoelastic element  $i = 1, \dots, m$ . Here, for simplicity, we assumed that  $\alpha = \alpha_\infty = \alpha_i$ , which reduced the number of independent parameters to  $2 + 2m$ . We identified these parameters using the nonlinear least-squares algorithm `lsqnonlin` in MATLAB. We optimized two distinct parameter sets to best represent the *unconditioned* response of the first loading cycle and the *conditioned* response of the third loading cycle. When identifying the parameters for the *conditioned* response, we evaluated the model for all three cycles. Yet, only the values of the third cycle entered the parameter identification. To evaluate the suitability of different loading conditions for the parameter identification, we first calibrated the viscoelastic model separately with the average experimental data from each loading mode—simple shear, shear relaxation, unconfined compression, compression relaxation, and unconfined tension—to obtain one set of material parameters per loading mode. We minimized the objective function,

$$\chi^2 = \sum_{i=1}^n [P_{az} - P_{az}^\psi]^2, \tag{24}$$

where  $n$  is the number of considered experimental data points indicated by the black dots in Figs. 3 and 5.  $P_{az}$  and  $P_{az}^\psi$  with directions  $a = \{x, y, z\}$  are the experimentally measured and computationally predicted Piola stresses. Since the shear modulus can only adopt positive values, we constrained it to  $\mu_\infty > 0$  and  $\mu_i > 0$ . In the next step, we simultaneously considered all five loading conditions for the calibration using the objective function

$$\chi^2 = \sum_{i=1}^{n_s+n_{sr}} [P_{xz} - P_{xz}^\psi]^2 + \sum_{i=1}^{n_c+n_{cr}+n_t} [P_{zz} - P_{zz}^\psi]^2, \tag{25}$$

where  $n_s, n_{sr}, n_c, n_{cr}$ , and  $n_t$  are the numbers of experimental data points for shear, shear relaxation, compression, compression relaxation, and tension.

When identifying the material parameters for combined compression/tension-shear loading with Protocol 2 in Table 2, we fitted the shear stresses of all shear curves for eleven axial stretch levels simultaneously, and minimized the objective function

$$\chi^2 = \sum_{k=1}^{11} \sum_{i=1}^n [P_{xz,k} - P_{xz}^\psi(\lambda_k)]^2, \tag{26}$$

where  $\lambda_k = \{1.00, 0.95, 0.90, 0.85, 0.80, 0.75, 1.05, 1.10, 1.15, 1.20, 1.25\}$ . To evaluate the ‘goodness of fit’, we determined the coefficient of determination,  $R^2 = 1 - P^{res}/P^{tot}$ , where  $P^{res} = \sum_{i=1}^n [P_i - P_i^\psi]^2$  is the sum of the squares of the residuals with the experimental data  $P_i$ , the corresponding model data  $P_i^\psi$ , and the number of data points  $n$ , and  $P^{tot} = \sum_{i=1}^n [P_i - \bar{P}]^2$  is the total sum of squares with the mean of the experimental data  $\bar{P} = 1/n \sum_{i=1}^n P_i$ .

### 3. Results

#### 3.1. Prony series

Fig. Fig. 2 illustrates the characteristic stress relaxation behavior in shear and compression with the Prony series model for different brain regions, the cortex, the basal ganglia, the corona radiata, and the corpus callosum. The Prony series assumes that the time-dependency follows a reduced relaxation function  $G(t) = [1 - \sum_{i=1}^n g_i [1 - \exp - t/\tau_i]]$  with the characteristic relaxation times  $\tau_i$  and the relaxation coefficients  $g_i$ . It is often referred to as Fung’s theory (Fung, 1993) or quasi-linear viscoelasticity (QLV). For comparison with previous experimental studies, we determined the characteristic time constants  $\tau_i$  by approximating the scaled relaxation behavior assuming instantaneous loading. Based on our recent results of human brain tissue (Budday et al., 2017b), we used a two-term Prony series.

**Table 3**  
Characteristic time constants  $\tau_i = \eta_i/\mu_i$  for Prony series approach of shear relaxation and compression relaxation.

	shear relaxation			compression relaxation		
	$\tau_1$ [s]	$\tau_2$ [s]	$R^2$ [s]	$\tau_1$ [s]	$\tau_2$ [s]	$R^2$ [s]
C	1.81	61.80	0.978	4.07	88.91	0.996
BG	1.58	44.56	0.973	3.98	83.01	0.994
CR	1.06	46.58	0.969	3.16	73.45	0.993
CC	1.09	46.76	0.951	2.80	81.85	0.994

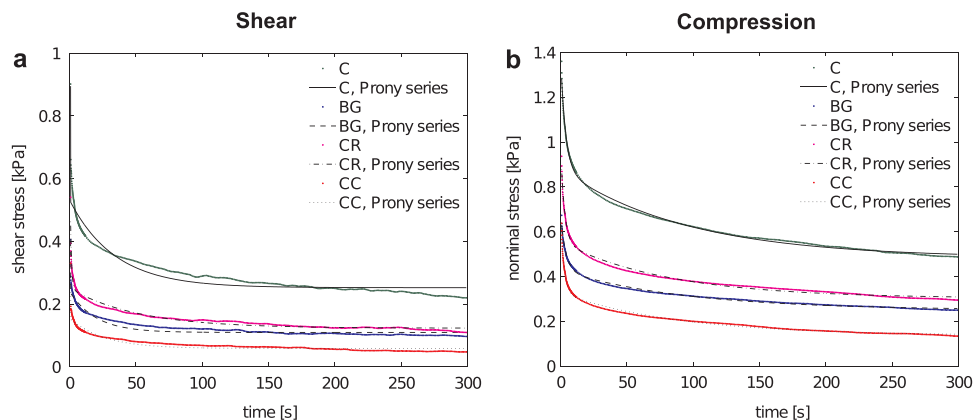
Table 3 summarizes the two time constant  $\tau_1$  and  $\tau_2$  for different brain regions. The shorter time constant  $\tau_1$ , which we associate with fluid flow within the cell as illustrated in Fig. 1b, shows similar regional trends for shear and compression loading. The cells in the white matter, the corona radiata and the corpus callosum, responded faster than in the gray matter, the cortex and the basal ganglia. The second time constant is largest for the cortex, similar to the first one, while we do not observe a clear trend for all other brain regions. All time constants are generally larger for compression than for shear loading. Notably, we observed a marked sensitivity of the time constants with respect to the experimental data, not only for the absolute values but also for regional trends, especially for the longer time scale. To address this sensitivity, we used more data points in the early relaxation up to 50 s as indicated by the dots in Fig. 2. This allowed us to eliminate a generally observed drawback of the Prony series, the correlation of the time constants  $\tau$  to the holding time of the relaxation experiment (de Rooij and Kuhl, 2016).

#### 3.2. Sensitivity of viscoelastic material parameters towards loading mode

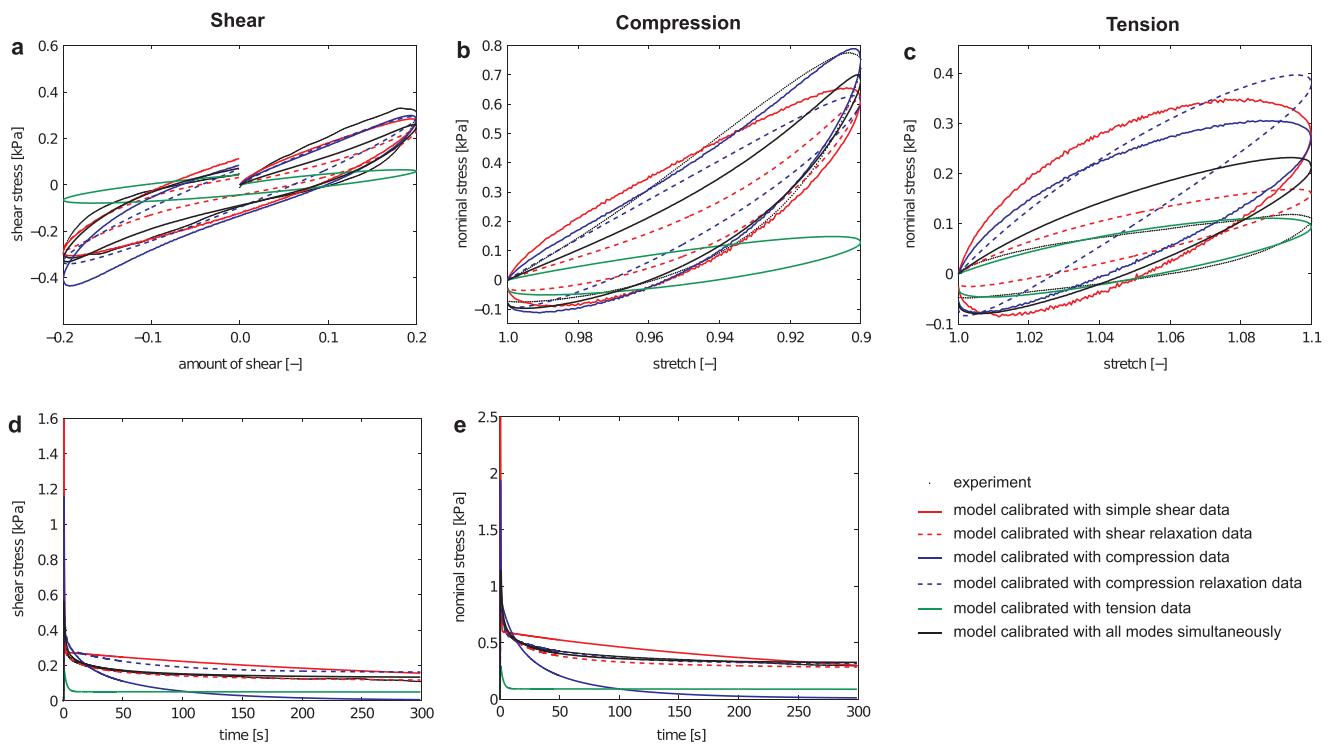
Fig. Fig. 3 compares the performance of our viscoelastic model from Section 2.3 calibrated using the *unconditioned* response of each loading mode separately by minimizing the objective function (24) against using all loading conditions simultaneously with the objective function (25). Here, we illustrate this comparison exemplarily for the corona radiata.

Fig. Fig. 4 illustrates the experimental data during the first loading cycle associated with the *unconditioned* response in all four regions, the cortex (C,  $n = 13$ ), the basal ganglia (BG,  $n = 15$ ), the corona radiata (CR,  $n = 19$ ), and the corpus callosum (CC,  $n = 11$ ) together with the corresponding constitutive model calibrated using data from all five loading modes simultaneously.

Table 4 summarizes the corresponding material parameters and coefficients of determination for all four regions calibrated using data from each loading mode separately and from all loading modes



**Fig. 2.** Average experimental data and two-term Prony series model for shear relaxation (a) and compression relaxation (b) in four brain regions, the cortex (C,  $n = 13$ ), the basal ganglia (BG,  $n = 15$ ), the corona radiata (CR,  $n = 19$ ), and the corpus callosum (CC,  $n = 11$ ), see Table 3.



**Fig. 3.** Sensitivity of parameter identification with respect to loading mode. Average experimental data during the first loading cycle associated with the *unconditioned* response during simple shear (a), compression (b), tension (c), shear relaxation (d), and compression relaxation (e), shown for specimens from the corona radiata, with corresponding constitutive models calibrated using data from each loading mode separately and all loading modes simultaneously, see Table 4.

simultaneously. Evidently, the cyclic data alone fail to satisfactorily calibrate the model with two viscoelastic modes, and cannot appropriately represent both early and late relaxation. Here, simple shear experiments showed a better performance than cyclic compression and tension since they were the longest experiments with a total duration of

50 s compared to only 20 s for compression or tension. The parameters from the tension data alone drastically underestimated the compressive stresses. Parameters calibrated from either compression or tension failed to depict the pronounced compression-tension asymmetry, which is well apparent when comparing graphs 3b and 3c. Shear relaxation

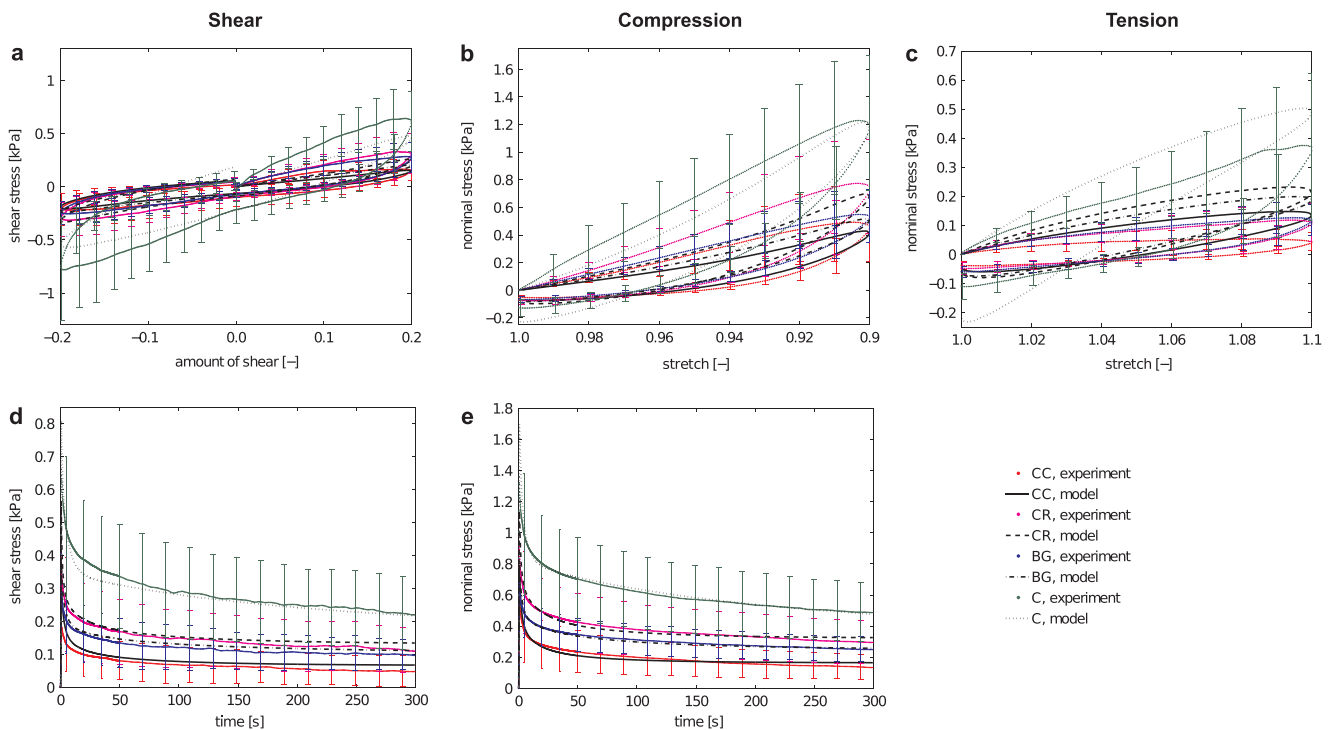


**Fig. 4.** Simultaneous parameter identification for all five loading modes. Average experimental data during the first loading cycle associated with the *unconditioned* response, with standard deviations indicated by the error bars, in four regions, cortex (C,  $n = 13$ ), basal ganglia (BG,  $n = 15$ ), corona radiata (CR,  $n = 19$ ), and corpus callosum (CC,  $n = 11$ ), with corresponding constitutive model calibrated using data from all loading modes simultaneously, see Table 4.

**Table 4**

Viscoelastic parameters and coefficients of determination calibrated with the averaged *unconditioned* response in four brain regions, the cortex (C,  $n=13$ ), the basal ganglia (BG,  $n=15$ ), the corona radiata (CR,  $n=19$ ), and the corpus callosum (CC,  $n=11$ ), for different loading modes separately, shear, compression, tension, shear relaxation, and compression relaxation, and all modes simultaneously.

<i>unconditioned</i> response	$\mu_\infty$ [kPa]	$\alpha$ [-]	$\mu_1$ [kPa]	$\eta_1$ [kPa·s]	$\mu_2$ [kPa]	$\eta_2$ [kPa·s]	$R_s^2$ [-]	$R_{sr}^2$ [-]	$R_c^2$ [-]	$R_{cr}^2$ [-]	$R_t^2$ [-]
simple shear											
C	0.01	-16.25	22.94	4.09	2.33	148.23	0.979	-5.06	0.911	-6.05	-0.72
BG	0.90	-7.53	13.46	3.49	0.17	20957.81	0.975	-12.77	0.967	-9.59	-3.20
CR	0.01	-9.97	15.09	3.67	1.18	873.24	0.973	-6.73	0.964	-2.96	-6.84
CC	0.01	-4.70	7.67	2.08	0.85	42.35	0.976	-4.84	0.897	-1.85	-9.54
shear relaxation											
C	0.61	-18.71	1.28	2.40	0.80	138.38	0.821	0.979	0.890	0.882	0.825
BG	0.24	-20.97	0.70	1.00	0.31	43.98	0.828	0.966	0.835	0.934	0.765
CR	0.29	-21.47	1.26	1.00	0.40	56.61	0.842	0.975	0.770	0.943	0.332
CC	0.11	-20.06	0.76	1.00	0.24	47.09	0.719	0.937	0.645	0.824	0.059
compression											
C	0.01	-11.92	14.93	3.46	2.17	314.92	0.941	-1.54	0.997	-2.19	-0.29
BG	0.01	-12.73	5.27	2.14	0.99	116.44	0.944	-2.37	0.997	-3.04	-1.05
CR	0.01	-16.77	8.48	2.39	1.24	93.37	0.916	-2.84	0.992	-2.54	-4.26
CC	0.01	-20.35	5.99	1.62	0.75	39.81	0.924	-4.03	0.987	-1.95	-4.98
compression relaxation											
C	1.12	-6.64	1.29	4.04	0.95	97.16	0.890	0.954	0.910	0.993	-0.58
BG	0.65	-3.93	0.69	1.97	0.47	36.72	0.915	0.494	0.933	0.988	-3.06
CR	0.79	-4.05	1.26	2.36	0.67	44.29	0.914	0.514	0.916	0.985	-9.68
CC	0.26	-10.89	0.85	1.81	0.39	47.17	0.894	0.580	0.860	0.989	-4.89
tension											
C	0.80	-0.00	0.78	1.50	0.80	1.56	0.556	-0.660	0.133	-1.97	0.970
BG	0.14	-0.00	0.74	2.08	0.12	278.91	0.534	-1.14	-0.02	-3.58	0.992
CR	0.19	-0.00	0.77	1.50	0.07	206.60	0.436	-1.55	-0.22	-3.54	0.990
CC	0.04	-0.01	0.44	1.50	0.01	529.11	0.298	-1.40	-0.26	-2.51	0.985
all modes											
C	0.36	-16.07	1.78	10.18	0.82	697.88	0.922	0.963	0.954	0.861	0.308
BG	0.33	-17.23	0.79	2.89	0.29	48.71	0.915	0.882	0.945	0.895	0.318
CR	0.35	-20.80	1.18	2.51	0.41	40.72	0.936	0.915	0.915	0.897	-0.71
CC	0.17	-21.41	0.78	1.91	0.30	22.85	0.907	0.678	0.894	0.905	-1.77

**Table 5**

Characteristic time constants  $\tau_i = \eta_i/\mu_i$  calibrated with the *unconditioned* response of each loading mode separately and for all loading modes simultaneously.

<i>unconditioned</i> response	shear cyclic		shear relaxation		compression cyclic		compression relaxation		tension cyclic		all modes	
	$\tau_1$ [s]	$\tau_2$ [s]	$\tau_1$ [s]	$\tau_2$ [s]	$\tau_1$ [s]	$\tau_2$ [s]	$\tau_1$ [s]	$\tau_2$ [s]	$\tau_1$ [s]	$\tau_2$ [s]	$\tau_1$ [s]	$\tau_2$ [s]
C	0.18	63.54	1.87	173.18	0.23	145.26	3.14	101.79	1.93	1.94	5.73	849.85
BG	0.26	126824.54	1.42	143.57	0.40	117.22	2.87	78.85	2.81	2304.78	3.65	167.53
CR	0.24	741.61	0.80	142.79	0.28	75.02	1.87	66.59	1.96	2781.62	2.12	99.48
CC	0.27	49.82	1.32	193.61	0.27	52.76	2.14	119.87	3.44	51946.26	2.46	77.37

experiments were the most suitable to obtain parameters that were valid under various loading modes. We note, though, that in contrast to the Prony series approach in the previous Section, we evaluated the full integral over the entire loading history including the loading ramp, instead of assuming an instantaneous loading. This helped significantly to reduce the sensitivity of the time constants towards the selection of experimental data points and additionally provided a reasonable identification of the elastic parameters. We achieved an even better agreement with experimental data when we calibrated the viscoelastic model with all loading conditions simultaneously. The resulting set of six parameters is not only valid for a single loading mode, but for arbitrary loading conditions. With the chosen framework, the parameters are conform with many commercial finite element software including

Abaqus. This was not possible for our previously provided parameter sets, for which we used different parameters  $\alpha_\infty$  and  $\alpha_i$  for the equilibrium and non-equilibrium responses (Budday et al., 2017b). Independent of the loading mode, the equilibrium shear moduli were largest in the cortex, comparable in basal ganglia and corona radiata, and smallest in the corpus callosum, which is in agreement with previous studies (Budday et al., 2017ab). We observed similar trends for shear moduli associated with large viscosities  $\eta_i$ . For shear moduli associated with small viscosities  $\eta_i$ , however, regional trends shifted: Both white matter regions stiffened with respect to the gray matter regions (Budday et al., 2017b), which becomes clearly apparent for  $\mu_1$  calibrated with shear or compression relaxation experiments. Shear relaxation experiments indicated the largest nonlinearity with large

absolute values of  $\alpha$  closely followed by cyclic unconfined compression, while tension experiments showed the smallest nonlinearity.

Table 5 summarizes the loading-mode-specific time constants  $\tau_i = \eta_i/\mu_i$  for the *unconditioned* tissue response in all four regions. Again, it becomes well apparent that cyclic experiments alone fail to provide reasonable time constants. They partially adopt extremely large values, since the experimental time was too short. As a result, the corresponding time constants reveal no clear regional trends. Yet, both relaxation experiments show similar regional trends: the first time constant  $\tau_1$  is largest in the cortex, slightly smaller in the basal ganglia, followed by the corpus callosum, and smallest in the corona radiata; the second time constant  $\tau_2$  is largest in the corpus callosum, followed by the cortex, the basal ganglia, and again smallest in the corona radiata. This suggests that, at small time scales, the corona radiata stiffens significantly compared to the other brain regions. Interestingly, the second time constants were larger for shear relaxation than for compression relaxation, while the first time constants showed the opposite trend. The parameters calibrated with all loading modes simultaneously show similar trends as the stress relaxation experiments with the exception that the second time constant was much smaller for the corpus callosum than for all other regions. We attribute this observation to the fact that the recorded tensile forces for the corpus callosum were in the range of the sensitivity of the force sensor.

Fig. 5 compares the performance of the viscoelastic model calibrated using the *conditioned* experimental data of each loading mode separately by minimizing the objective function (24) against using all loading conditions simultaneously by minimizing the objective function (25). Again, we illustrate this comparison exemplarily for the corona radiata.

Fig. 6 illustrates the experimental data during the third loading cycle associated with the *conditioned* response in all four regions, the cortex (C,  $n = 13$ ), the basal ganglia (BG,  $n = 15$ ), the corona radiata (CR,  $n = 19$ ), and the corpus callosum (CC,  $n = 11$ ) together with the corresponding constitutive model calibrated using data from all five loading modes simultaneously.

Table 6 summarizes the corresponding material parameters and coefficients of determination for all four regions. Even for the *conditioned* response, stress relaxation experiments provide better estimates for the material parameters with larger coefficients of determination  $R^2$  than cyclic experiments. We note that the relaxation data are the same for the *unconditioned* and *conditioned* parameter identification. Again, models calibrated with compression data only overestimate tensile stresses. Considering all loading modes simultaneously for calibration, we obtain a set of six material parameters that well represent the *conditioned* tissue response under all loading conditions performed during Protocol 1. The region-specific parameter sets can be used immediately for large scale simulations in commercial finite element software that use the multiplicative decomposition of the deformation gradient (5) such as Abaqus. The viscoelastic shear moduli  $\mu_1$  and  $\mu_2$  from the cyclic fits are smaller—only about half the value—for the *conditioned* than for the *unconditioned* response. This suggests that the fluid phase, which can escape the solid matrix during the initial loading, adds further resistance to load. When we identify the parameters with all loading conditions simultaneously, this effect is less pronounced. As expected, the equilibrium shear moduli are only marginally affected by conditioning. Interestingly, the *conditioned* response is more non-linear than the *unconditioned* response with larger absolute values of  $\alpha$ . This suggests that the nonlinearity can be attributed to the solid matrix rather than to the fluid phase.

Table 7 summarizes the loading-mode-specific time constants  $\tau_i = \eta_i/\mu_i$  for the *conditioned* response in all four regions. The time scales were generally larger compared to the *unconditioned* behavior, which we attribute to the fluid phase, which can be squeezed out during initial loading (also see Fig. 1b) and is no longer present in the later cycles. When we considered all loading conditions simultaneously for calibration, the first time constants were slightly larger for the *conditioned* than for the *unconditioned* response, but generally showed similar trends. The second time constants, in contrast, had significantly increased compared to the *unconditioned* response; this effect was more pronounced in white than in gray matter. This suggests that most fluid

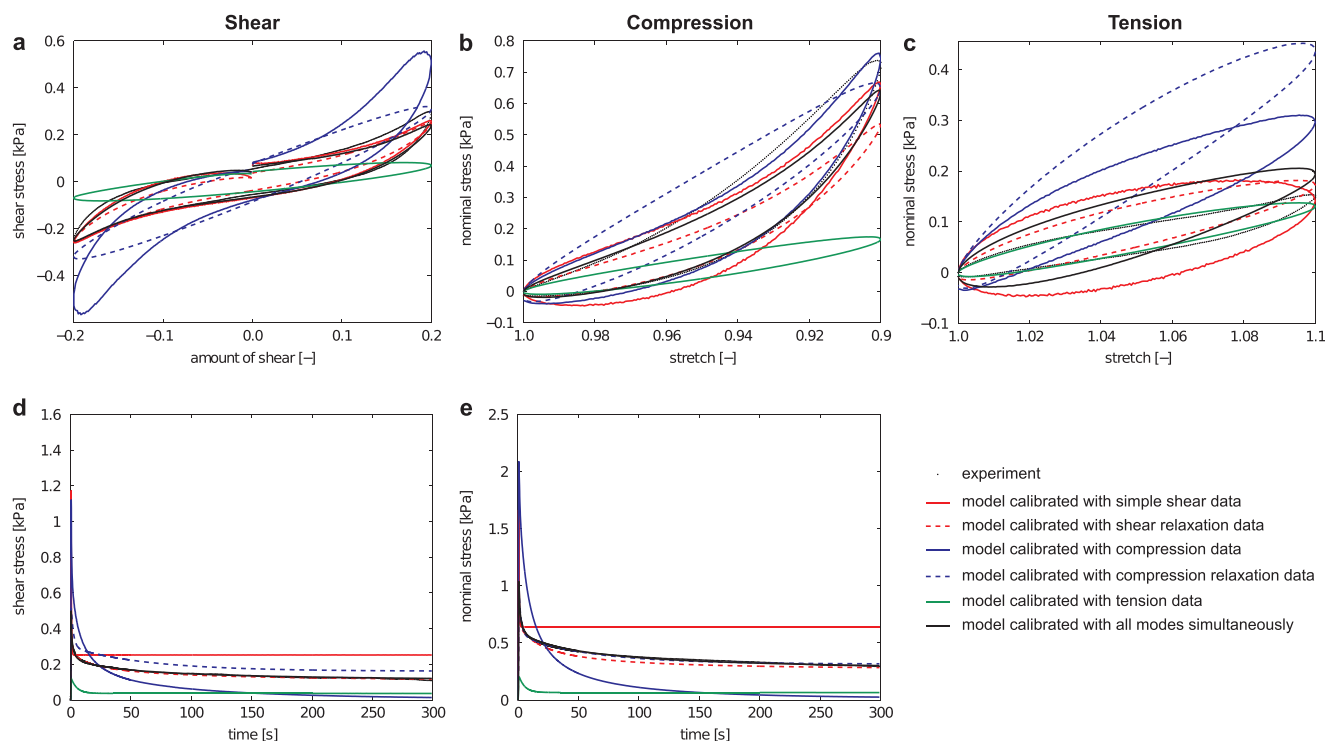
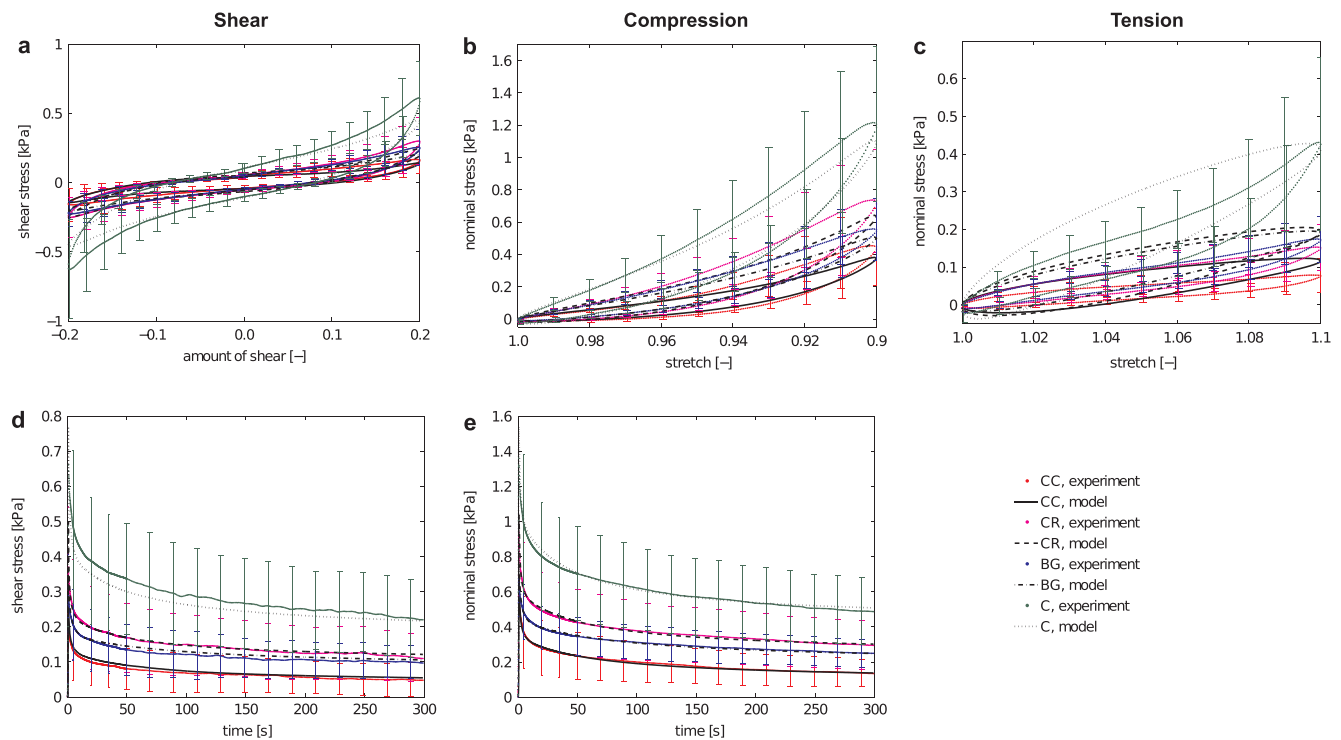


Fig. 5. Sensitivity of parameters identification with respect to loading mode. Average experimental data during the third loading cycle associated with the *conditioned* response during simple shear (a), compression (b), tension (c), shear relaxation (d), and compression relaxation (e), shown for specimens from the corona radiata, with corresponding constitutive models calibrated using data from each loading mode separately and all loading modes simultaneously, see Table 6.



**Fig. 6.** Simultaneous parameter identification for all five loading modes. Average experimental data during the third loading cycle associated with the *conditioned* response, with standard deviations indicated by the error bars, in four regions, cortex (C,  $n = 13$ ), basal ganglia (BG,  $n = 15$ ), corona radiata (CR,  $n = 19$ ), and corpus callosum (CC,  $n = 11$ ), with corresponding constitutive model calibrated using data from all loading modes simultaneously, see Table 6.

escaped from specimens of the corpus callosum followed by those from the corona radiata; gray matter specimens from the cortex seem to loose the least fluid during the first cycle.

### 3.3. Combined loading

Fig. 7 shows the average *unconditioned* shear stress versus the amount of shear for specimens from the corona radiata. The graph summarizes the combined compression/tension-shear response for all eleven stretch levels according to Protocol 2 in Table 2 calibrated by minimizing the objective function (26). Our model is capable of capturing the increase in shear stresses with increasing compression, but much less with increasing tension, which is the natural outcome of the compression-tension asymmetry observed in Figs. 3 and 5. It underestimates stresses during the initial loading (Budday et al., 2017b), but agrees well with the experimental data after that. We believe that the marked decrease in shear stresses from 0% to 5% tension is rather an artifact of the test setup than an inherent tissue characteristic. We unavoidably *conditioned* the tissue during compression-shear loading, which might have led to a slight drop in shear stresses for the first tension level compared to the initial loading. To avoid this artifact, we could have tested each specimen under a single strain level only. However, with the large inter-specimen variation observed for brain tissue in general, this would have required a large number of samples to provide statistically meaningful results.

Table 8, top, summarizes the material parameters for the *unconditioned* response. Calibrating the viscoelastic constitutive model with all axial stretch levels during combined loading simultaneously yielded a larger equilibrium modulus  $\mu_\infty$  than the simultaneous fit of all uniaxial loading modes in Table 4, bottom. This can be associated with the much smaller absolute value of  $\alpha$ ; a large absolute value of  $\alpha$  as the one obtained from Protocol 1 would yield unrealistically large shear stresses for large compressive or tensile pre-strain in the combined loading case. Similar to the parameter estimates from the cyclic

experiments in Table 4, the cyclic combined compression/tension-shear tests are not sufficient to accurately characterize the long-term time parameters. Consequently, the larger viscosity adopts an unrealistically large value. While we achieve coefficients of determination close to one for the combined loading tests in Fig. 7, the corresponding predictions for the uniaxial loading at smaller strains in Protocol 1 are relatively poor, which becomes apparent through smaller  $R^2$  values in Table 8, top. We note, though, that Protocol 1 was not performed on the same specimens as Protocol 2, which implies that we can not exclude possible influences of inter-specimen variations.

Fig. 8 shows the average *conditioned* shear stress versus amount of shear curves during all eleven stretch levels of combined compression/tension-shear loading according to Protocol 2. Again, the model captures the increase in shear stresses accompanied by an increase in hysteresis area with increasing compression, but not with increasing tension. The fact that the opening of the hysteresis at zero shear increases with axial compression, but not with axial tension, suggests that the experimentally observed increase in shear stresses in tension is in part an artifact of the testing method rather than an inherent characteristic of the tissue. The time required to complete the combined loading protocol was exceptionally long and it was difficult to keep the tissue fully hydrated; samples dried out towards the end of the testing period, which led to an artificial increase in stresses for the axial stretch levels that we probed last. This could also explain why the increase in shear stresses with axial tension is more pronounced in the current study than in previous experimental studies on mouse brain tissue (Pogoda et al., 2014).

Table 9, top, summarizes the corresponding material parameters for the *conditioned* tissue response. Again, the absolute value of the non-linearity parameter  $\alpha$  is much smaller than estimated from the uniaxial loading cases in Protocol 1, but it is slightly larger than for the *unconditioned* response in Table 8, top. The viscosities seem more realistic than those obtained for the *unconditioned* response.

**Table 6**

Viscoelastic parameters and coefficients of determination calibrated with the averaged *conditioned* response in four brain regions, the cortex (C,  $n = 13$ ), the basal ganglia (BG,  $n = 15$ ), the corona radiata (CR,  $n = 19$ ), and the corpus callosum (CC,  $n = 11$ ), for different loading modes separately, shear, compression, tension, shear relaxation, and compression relaxation, and all modes simultaneously.

<i>conditioned</i> response	$\mu_\infty$ [kPa]	$\alpha$ [-]	$\mu_1$ [kPa]	$\eta_1$ [kPa·s]	$\mu_2$ [kPa]	$\eta_2$ [kPa·s]	$R_s^2$ [-]	$R_{sr}^2$ [-]	$R_c^2$ [-]	$R_{cr}^2$ [-]	$R_t^2$ [-]
simple shear											
C	0.37	-28.74	12.70	2.03	0.99	43.67	0.949	-0.30	0.858	-0.76	0.644
BG	0.52	-20.82	6.52	2.17	0.08	22405.38	0.931	-4.12	0.972	-4.88	0.031
CR	0.52	-25.00	8.52	2.17	0.01	20063.23	0.887	-2.08	0.888	-1.81	-0.32
CC	0.36	-19.13	3.48	1.71	0.07	8466.82	0.825	-2.56	0.879	-1.04	-3.13
shear relaxation											
C	0.61	-18.72	1.28	2.40	0.80	138.33	0.830	0.980	0.885	0.882	0.175
BG	0.24	-20.99	0.71	1.00	0.31	44.03	0.842	0.967	0.782	0.934	0.373
CR	0.29	-21.47	1.26	1.00	0.40	56.61	0.842	0.979	0.692	0.943	-0.37
CC	0.11	-20.08	0.76	1.00	0.24	47.17	0.716	0.941	0.617	0.824	-1.32
compression											
C	0.01	-28.08	1.71	5.71	0.78	256.46	0.862	-0.23	0.923	-1.08	-0.23
BG	0.01	-25.71	0.84	4.63	0.34	270.55	0.934	0.517	0.937	-0.20	-1.89
CR	0.01	-28.77	3.66	1.50	1.17	122.02	0.774	-3.27	0.919	-5.19	-5.75
CC	0.01	-50.00	0.70	3.61	0.07	71.82	0.816	-0.93	0.859	-1.57	-5.06
compression relaxation											
C	1.12	-6.63	1.29	4.04	0.95	97.18	0.899	0.955	0.859	0.993	-2.94
BG	0.66	-3.92	0.69	1.97	0.47	36.73	0.936	0.487	0.873	0.988	-6.56
CR	0.79	-4.06	1.26	2.36	0.66	44.29	0.915	0.512	0.876	0.985	-17.7
CC	0.26	-10.90	0.85	1.81	0.39	47.14	0.886	0.578	0.849	0.989	-11.6
tension											
C	0.62	-0.16	0.44	1.52	0.45	1.63	0.534	-1.41	0.179	-3.01	0.669
BG	0.06	-0.02	0.56	5.09	0.01	308.90	0.652	-2.63	0.195	-5.47	0.343
CR	0.14	-0.01	0.45	2.12	0.05	355.96	0.497	-2.08	-0.07	-4.13	0.431
CC	0.01	-0.08	0.30	1.55	0.04	529.01	0.351	-1.60	-0.10	-2.68	0.198
all modes											
C	0.52	-20.47	1.35	2.92	0.62	144.67	0.804	0.935	0.879	0.962	0.371
BG	0.22	-21.27	0.61	2.44	0.25	128.48	0.890	0.946	0.890	0.954	-0.40
CR	0.18	-27.53	0.87	2.45	0.24	151.78	0.872	0.963	0.827	0.948	-0.90
CC	0.05	-30.64	0.54	1.92	0.14	141.71	0.760	0.897	0.748	0.972	-1.82

3.4. Optimized material parameters for larger loading

Since experimental evidence suggests that the viscosity of brain tissue is independent of the deformation (Budday et al., 2017b; Labus and Puttlitz, 2016), we assumed that the viscosities calibrated with Protocol 1 were also valid for the combined loading cases with Protocol 2. To optimize the parameters in Section 3.3, we used the information from stress relaxation experiments in the corona radiata in Tables 4 and 6: We set  $\eta_1 = 2.5$  s and  $\eta_2 = 40$  s for the *unconditioned* tissue response, and  $\eta_1 = 2.5$  s and  $\eta_2 = 150$  s for the *conditioned* tissue response. Then we re-ran the parameter optimization for the remaining four parameters.

Figs. 9 and 10 show the performance of the optimized model to capture the *unconditioned* and *conditioned* behavior during uniaxial shear, compression, and tension according to Protocol 1, and during combined compressen/tension-shear according to Protocol 2. Figs. 8 and 9, bottom, summarize the corresponding constitutive parameters. The model still underestimates stresses in shear and compression for small strains during Protocol 1 as illustrated in Figs. Figs. 9a–b and 10a–b. However, the qualitative stress relaxation behavior is much better captured compared to the material parameters in Figs. 8 and 9, top. Even though this is not directly apparent through the coefficients of determination  $R^2$ , it will ensure that the relaxation at larger strains will be adequately predicted. Furthermore, the optimized approach ensures

**Table 7**

Characteristic time constants  $\tau_i = \eta_i/\mu_i$  calibrated with the *conditioned* response of each loading mode separately and for all loading modes simultaneously.

<i>conditioned</i> response	shear cyclic		shear relaxation		compression cyclic		compression relaxation		tension cyclic		all modes	
	$\tau_1$ [s]	$\tau_2$ [s]	$\tau_1$ [s]	$\tau_2$ [s]	$\tau_1$ [s]	$\tau_2$ [s]	$\tau_1$ [s]	$\tau_2$ [s]	$\tau_1$ [s]	$\tau_2$ [s]	$\tau_1$ [s]	$\tau_2$ [s]
C	0.16	44.28	1.87	173.15	3.34	328.12	3.14	101.80	3.46	3.64	2.17	235.07
BG	0.33	291561.25	1.42	143.83	5.49	802.43	2.87	78.87	9.07	30360.59	3.97	520.41
CR	0.25	2006278.35	0.80	142.78	0.41	103.86	1.87	66.60	4.71	7781.03	2.82	644.80
CC	0.49	125151.51	1.32	194.14	5.18	1035.19	2.14	119.83	5.17	14306.23	3.58	1039.17

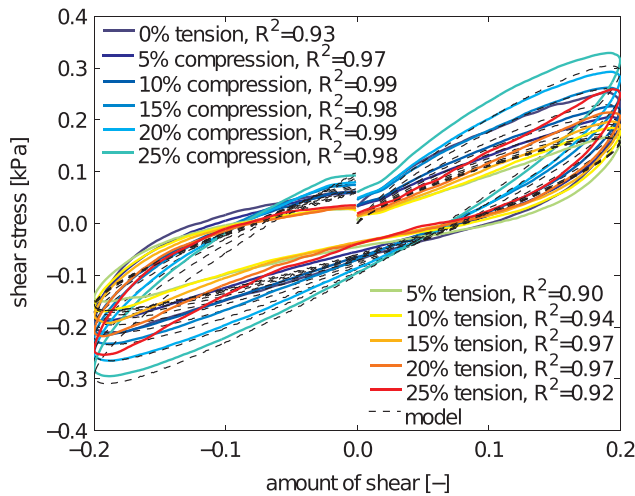


**Fig. 7.** Unconditioned response during combined compression/tension-shear. Sinusoidal simple shear superimposed on axial stretch with  $\lambda = 1.0$  ( $n = 8$ ),  $0.95$  ( $n = 8$ ),  $0.9$  ( $n = 8$ ),  $0.85$  ( $n = 8$ ),  $0.8$  ( $n = 8$ ),  $0.75$  ( $n = 8$ ),  $1.05$  ( $n = 8$ ),  $1.1$  ( $n = 8$ ),  $1.15$  ( $n = 8$ ),  $1.2$  ( $n = 8$ ), and  $1.25$  ( $n = 5$ ). Experiments (solid lines) and viscoelastic model (dashed lines) with parameters from Table 8, top. The model captures the pronounced increase in shear stresses with increasing compressive strain and the less pronounced increase in shear stresses with increasing tensile strain.

that the predicted opening of the hysteresis for cyclic simple shear at zero shear in Fig. Fig. 10a agrees well with the experiment.

#### 4. Discussion

Material parameters for brain tissue are commonly reported for a single loading mode, usually shear (Shuck and Advani, 1972; Donnelly and Medige, 1997; Bilston et al., 2001; Rashid et al., 2013; Destrade et al., 2015) or compression (Rashid et al., 2012), and sometimes tension (Labus and Puttlitz, 2016; Miller and Chinzei, 2002; Rashid et al., 2014). Yet, under physiological conditions, the living brain rarely sees a single loading mode in pure isolation. Rather, it is exposed to a combination of shear, compression, and tension and a wide range of loading rates. To characterize the response of the brain under combined loading, we modeled brain tissue using a finite strain Ogden type viscoelastic model with six material parameters: one elastic and two viscoelastic stiffnesses  $\mu_\infty$ ,  $\mu_1$ , and  $\mu_2$ , a single non-linearity parameter  $\alpha$ , and two viscoelastic time constants  $\eta_1$  and  $\eta_2$ . In contrast to our previous model with three different non-linearity parameters  $\alpha_\infty$ ,  $\alpha_1$ , and  $\alpha_2$  (Budday et al., 2017b), the current formulation now allows us to directly adopt finite element software packages such as Abaqus, where the viscoelastic formulation uses a single, unified non-linearity parameter  $\alpha$ . Although our current model has two parameters less than our initial model, its agreement with experimental data is almost identical to our previous model (Budday et al., 2017b). In this study, we identified the six model parameters for different regions in the human brain

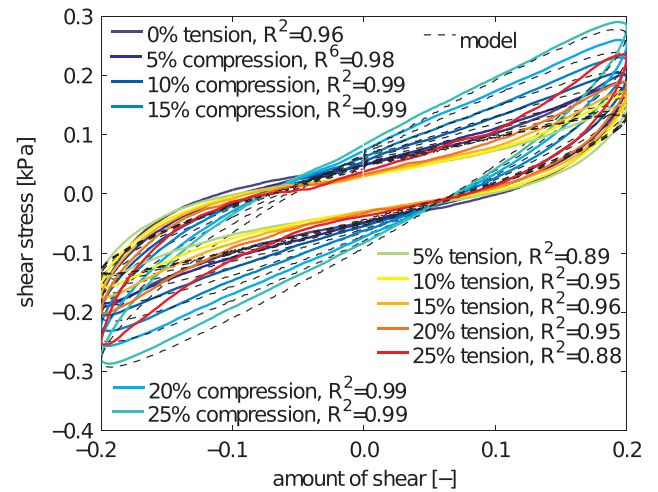


**Fig. 8.** Conditioned response during combined compression/tension-shear. Sinusoidal simple shear superimposed on axial stretch with  $\lambda = 1.0$  ( $n = 8$ ),  $0.95$  ( $n = 8$ ),  $0.9$  ( $n = 8$ ),  $0.85$  ( $n = 8$ ),  $0.8$  ( $n = 8$ ),  $0.75$  ( $n = 8$ ),  $1.05$  ( $n = 8$ ),  $1.1$  ( $n = 8$ ),  $1.15$  ( $n = 8$ ),  $1.2$  ( $n = 8$ ), and  $1.25$  ( $n = 5$ ). Experiments (solid lines) and viscoelastic model (dashed lines) with parameters from Table 9, top. The model captures the pronounced increase in shear stresses with increasing compressive strain and the less pronounced increase in shear stresses with increasing tensile strain.

under multiple loading conditions, both individually and simultaneously.

We note that despite some promising results, our method has several inherent limitations. First, by the very nature of triaxial testing, gluing the sample to the specimen holder may induce boundary effects and the deformation might not be as homogeneous as we had assumed. Yet, this effect seems to be more pronounced in tension and compression, rather than in simple shear (Rashid et al., 2013). In accordance with the literature (Destrade et al., 2015), we verified computationally that—for our chosen constitutive model, parameterized with our parameter set—the deformation was mainly homogeneous and boundary effects remained strictly local. Second, our goal was to complete all tests for each brain within a time window of 60 h post mortem. This posed practical limitations to the recovery time between the different tests and we can not guarantee that the results of individual tests were entirely independent of previous tests. Third, unfortunately, our current test setup does not allow us to characterize the poroelastic behavior of brain tissue. We are in the process of designing a combination of drained and un-drained experiments (Franceschini et al., 2006) to truly characterize brain as a poro-viscoelastic solid.

Our study confirms the general intuition that parameter sets, identified for a single loading condition and at a certain strain level, can considerably under- or overestimate the response under different loading conditions and at different strain levels. Of all three loading modes, shear, compression, and tension, our study showed that simple shear tests were better suited to characterize the ultra-soft response of

**Table 8**

Viscoelastic parameters and coefficients of determination calibrated with the averaged unconditioned response in the corona radiata (CR) for combined compression/tension-shear and optimized viscoelastic parameters and coefficients of determination calibrated with the averaged unconditioned response in the corona radiata (CR) for combined compression/tension-shear in combination with uniaxial experiments.

combined compression/tension-shear loading											
unconditioned response	$\mu_\infty$ [kPa]	$\alpha$ [-]	$\mu_1$ [kPa]	$\eta_1$ [kPa·s]	$\mu_2$ [kPa]	$\eta_2$ [kPa·s]	$R_s^2$ [-]	$R_{sr}^2$ [-]	$R_c^2$ [-]	$R_{cr}^2$ [-]	$R_t^2$ [-]
CR	0.74	-6.40	2.90	2.91	0.01	47931.27	0.853	0.472	0.644	0.163	-1.71
optimized constitutive parameters for large loading											
unconditioned response	$\mu_\infty$ [kPa]	$\alpha$ [-]	$\mu_1$ [kPa]	$\eta_1$ [kPa·s]	$\mu_2$ [kPa]	$\eta_2$ [kPa·s]	$R_s^2$ [-]	$R_{sr}^2$ [-]	$R_c^2$ [-]	$R_{cr}^2$ [-]	$R_t^2$ [-]
CR	0.69	-6.44	3.00	2.50	0.07	40.00	0.838	0.511	0.616	0.124	-1.25

**Table 9**

Viscoelastic parameters and coefficients of determination calibrated with the averaged *conditioned* response in the corona radiata (CR) for combined compression/tension-shear and optimized viscoelastic parameters and coefficients of determination calibrated with the averaged *conditioned* response in the corona radiata (CR) for combined compression/tension-shear in combination with uniaxial experiments.

combined compression/tension-shear loading											
<i>conditioned</i> response	$\mu_\infty$ [kPa]	$\alpha$ [-]	$\mu_1$ [kPa]	$\eta_1$ [kPa·s]	$\mu_2$ [kPa]	$\eta_2$ [kPa·s]	$R_s^2$ [-]	$R_{sr}^2$ [-]	$R_c^2$ [-]	$R_{cr}^2$ [-]	$R_t^2$ [-]
CR	0.01	-9.05	2.90	2.00	0.60	320.35	0.780	0.070	0.524	-1.00	-0.61
optimized constitutive parameters for large loading											
<i>conditioned</i> response	$\mu_\infty$ [kPa]	$\alpha$ [-]	$\mu_1$ [kPa]	$\eta_1$ [kPa·s]	$\mu_2$ [kPa]	$\eta_2$ [kPa·s]	$R_s^2$ [-]	$R_{sr}^2$ [-]	$R_c^2$ [-]	$R_{cr}^2$ [-]	$R_t^2$ [-]
CR	0.03	-11.00	0.61	2.50	0.47	150.00	0.787	-0.55	0.524	-1.90	-1.42

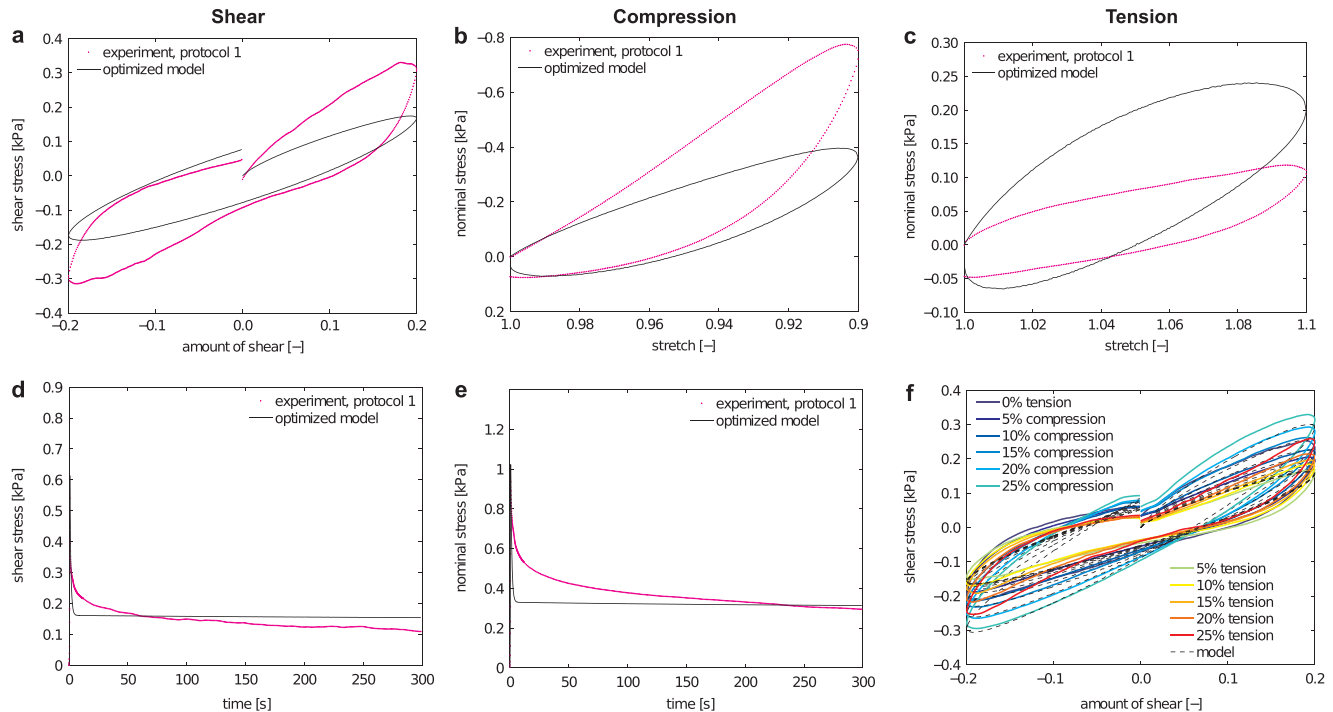


**Fig. 9.** Average *unconditioned* response during uniaxial simple shear (a), compression (b), tension (c), shear relaxation (d), compression relaxation (e), and combined compression/tension-shear (f) and optimized viscoelastic model with parameters from Table 8, bottom, in the corona radiata. We calibrated viscosities using uniaxial experiments (a–e) and elastic parameters using combined loading f.

brain tissue than compression or tension tests alone (Destrade et al., 2015). This agrees well with a recent study that argued that simple shear tests were more reliable, less sensitive to boundary effects, and more robust under large strains (Rashid et al., 2013). Of all five experiments, we found that shear relaxation experiments were best suited to identify the time-dependent material parameters. However, this was only true when the whole strain history—including the loading path—was included into the calibration. When fitting the reduced relaxation function and assuming an instantaneous loading (Miller and Chinzei, 1997; Rashid et al., 2012, 2014), the relaxation times became highly sensitive to the duration of the experiment and to the selection of data points for the fit (de Rooij and Kuhl, 2016). We observed that this sensitivity was greatly reduced when integrating over the entire loading history. More importantly, by including cyclic experiments into the fit, the parameter identification became less sensitive and more robust. Our findings agree well with a recent study on the viscoelasticity of the porcine corpus callosum during equibiaxial stress-relaxation (Labus and Puttlitz, 2016), which found that a major fraction of relaxation occurs during the initial loading period. This implies that Heaviside loading functions lead to poor predictions for elastic material parameters. To prevent these artifacts, we proposed a combined theoretical and

experimental approach that reliably identified both elastic and viscoelastic parameters using data from multiple loading conditions: Instead of calibrating the elastic parameters using only the loading path and the viscous parameters using only the stress relaxation behavior (Miller and Chinzei, 1997; Rashid et al., 2012; Forte et al., 2016), our approach integrates data from simple shear, unconfined compression, tension, shear relaxation, and compression relaxation to holistically characterize the overall behavior of gray and white matter tissue.

Unlike most soft tissues, the brain is not only ultrasoft, but also has an exceptionally high water content, 0.83 g/l in gray matter and 0.71 g/l in white matter (Whittall et al., 1997). This suggests that brain tissue is effectively poro-viscoelastic (Mehrabian and Abousleiman, 2011). Notably, we observed that both *unconditioned* viscous time constants were larger in gray matter with 6 s and 850 s than in white matter with 2 s and 99 s. Yet, both *conditioned* constants were smaller in gray matter with 2 s and 235 s than in white matter with 3 s and 645 s. These rheological differences suggest a different porosity between both tissues. We can rationalize these observations with the underlying tissue microstructure: The corona radiata consists of a sparsely cross-linked network of myelinated axons (Weickenmeier et al., 2017), whereas the cortex is made up of a densely connected network of

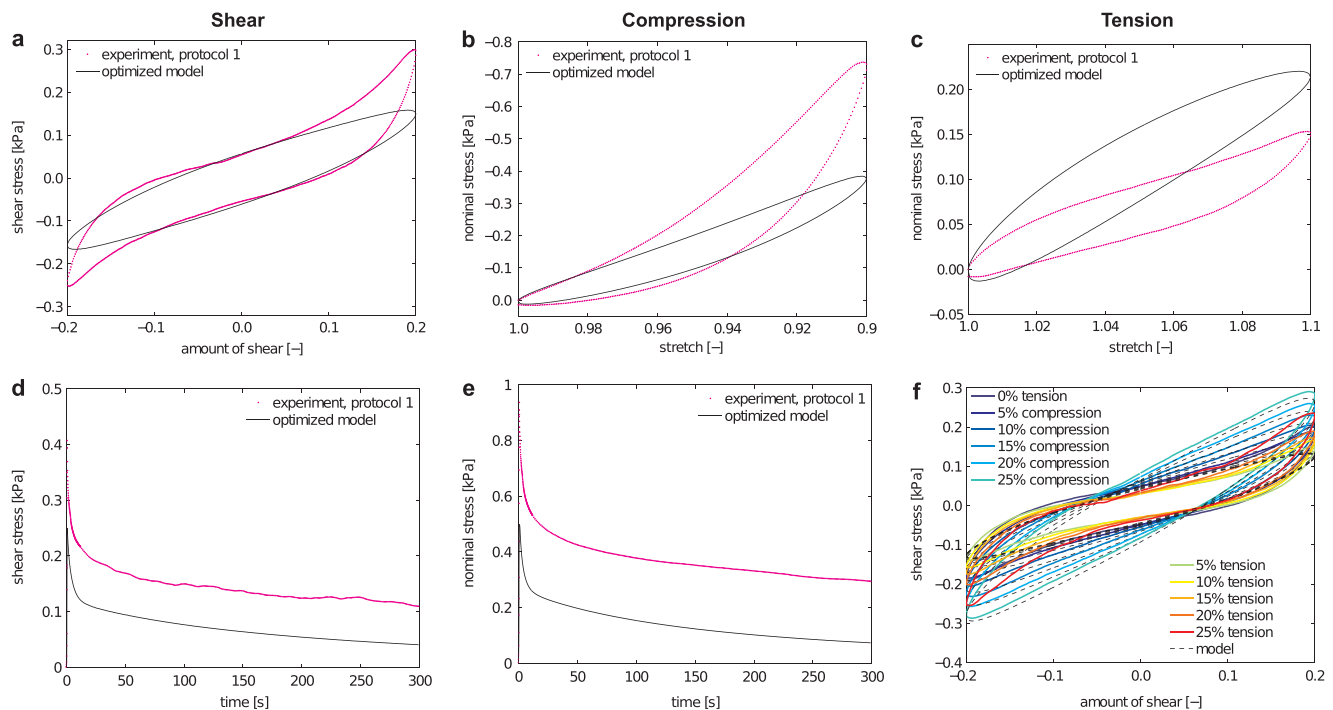


**Fig. 10.** Average *conditioned* response during uniaxial simple shear (a), compression (b), tension (c), shear relaxation (d), compression relaxation (e), and combined compression/tension-shear (f) and optimized viscoelastic model with parameters from Table 9, bottom, in the corona radiata. We calibrated viscosities using uniaxial experiments (a–e) and elastic parameters using combined loading f.

dendrites that traps the fluid phase inside the tissue. These differences could explain the ongoing discussion between reported stiffness differences in gray and white matter. Modeling the brain as a poro-viscoelastic solid and probing poro-viscoelasticity using drained and undrained experiments (Franceschini et al., 2006) would be critical to elucidate these time-dependent phenomena. Understanding the poro-viscoelasticity of the brain is important in the context of brain swelling (Lang et al., 2014) with pathological applications to edema (Goriely et al., 2015), hydrocephalus (Tully and Ventikos, 2011), or decompressive craniectomy (Goriely et al., 2016).

To discriminate between the initial loading cycle, with the porous fluid included, and repeated loading cycles, with the fluid partly squeezed out, we identified four distinct parameter sets associated with the *unconditioned* and *conditioned* responses at normal, physiological and elevated, pathological strain levels. While the unconditioned parameter set could be useful to mimic the *in vivo* conditions of fluid-saturated tissue in the living brain, the conditioned parameter set is easily reproducible under *ex vivo* conditions in the laboratory. To provide guidelines for simulations and comparisons for experimentalists, we view both data sets as rather independent, but valuable for their own class of applications. A challenge when performing several sequential tests on one and the same sample is to ensure sufficient recovery time between the individual tests, avoid tissue damage, and maintain tissue integrity during the course of the experiment. Here we restricted the maximum compressive and tensile stretches to  $\lambda = 0.9$  and  $\lambda = 1.1$  and the maximum shear to  $\gamma = 0.20$  to ensure that the tissue remained intact throughout all three loading modes. Our preliminary experiments had shown that larger strains permanently damaged the tissue. With a maximum compressive stretch of 0.9, we have previously shown that the tissue fully recovers and follows the initial loading path after a resting period of about one hour (Budday et al., 2017b). Some previous studies had identified parameters using the loading path—but not the unloading path—for up to 50% strain or more (Miller and Chinzei, 1997; Moran et al., 2014), which might be critical in view of tissue damage. The damage threshold for diffuse axonal injury, for example, has been reported at as low as 18% tensile strain (Bain and

Meaney, 2000). While smaller strain levels minimize damage throughout the course of the experiment, restricting the calibration to moderate strains has several other drawbacks: When comparing the calibration of the individual loading from Protocol 1 in Tables 4 and 6 with the calibration of the combined loading from Protocol 2, we found that the model overestimates the stress response at strains beyond the tested strain level; when calibrating the model with the combined loading from Protocol 2, in contrast, the model underestimates the stress response at moderate strains. This motivated us to combine the viscous parameters from Protocol 1 with the elastic parameters from Protocol 2. The associated optimized parameter sets for *unconditioned* and *conditioned* tissue seem to provide the best fit of the experimental data at finite strains. Their characteristic parameters are summarized in Tables 8 and 9, bottom.

Understanding cellular mechanisms and tissue microstructure is critical to interpret the constitutive behavior of the human brain. Here we have identified material parameters for each loading mode separately to better understand loading-mode specificity. This also allows us to correlate the parameters to the underlying mechanisms of load transfer within the tissue. Our findings strengthen our hypothesis that the rheology of brain tissue is characterized by at least two different time scales, one associated with the poroelastic interaction of the solid and fluid phases within the tissue and one related to the viscoelastic nature of the solid skeleton itself (Mehrabian and Abolesleiman, 2011). Further studies will be needed to explore the interplay of porosity and viscosity and their effects on brain tissue rheology both in time and space. We have already ruled out the possibility of permanent softening or irreversible damage as a possible interpretation for the observed time-dependent response (Franceschini et al., 2006). When re-testing the same sample after a resting period of 60 min, we observed that the behavior was fully reversible: The rested sample followed the identical loading path as the initial sample (Budday et al., 2017a).

## 5. Conclusion

We have shown that a finite viscoelastic Ogden model with an

elastic stiffness, two viscoelastic stiffnesses, a single unified non-linearity parameter, and two viscous time constants can characterize the experimental behavior of human brain tissue under multiple uniaxial and multiaxial loading conditions. Strikingly, parameters identified for a single loading mode can generate huge errors when used for a different mode of loading. These errors were smallest for parameters associated with shear relaxation experiments. This suggests that, of all loading modes, shear relaxation probes the broadest spectrum of material characteristics. When fitting our relaxation tests to the popular Prony series, we observed that the parameter identification was highly sensitive to the duration of the experiment and to the selection of data points for the fit. To address these limitations, we performed a combination of shear, shear relaxation, compression, compression relaxation, and tension tests and simultaneously identified sets of viscoelastic parameters for all five loading conditions. Altogether, we identified four distinct parameter sets associated with the *unconditioned* and *conditioned* responses at normal and elevated strain levels. In general, the elastic stiffness was on the order of 0.3 kPa, the viscoelastic stiffnesses were 1.0 kPa and 0.4 kPa, the nonlinearity parameter was on the order of  $-20$ , and the two viscous time constants were on the order of seconds and minutes. Notably, the *unconditioned* tissue was about one third stiffer than the *conditioned* tissue suggesting that porous fluid supports some of the initial load, but is then squeezed out throughout the first loading cycle. We believe that our parameter sets will be widely used for finite element simulations with custom-designed or commercial software packages such as Abaqus that feature Ogden type models at finite deformations. Our finite viscoelastic model is most applicable to simulate the response of the brain at moderate to long time scales with applications in neurodevelopment, neurooncology, neurosurgery, and neurodegeneration.

## Acknowledgements

The authors thank Dr. Johannes Haybaeck for providing the brain tissue samples. This study was supported by the German National Science Foundation grant STE 544/50 to SB and PS, and by the Humboldt Research Award to EK.

## References

- Bain, A.C., Meaney, D.F., 2000. Tissue-level thresholds for axonal damage in an experimental model of central nervous system white matter injury. *J. Biomech. Eng.* 122, 615–622.
- Bilston, L.E., Liu, Z., Phan-Thien, N., 2001. Large strain behaviour of brain tissue in shear: some experimental data and differential constitutive model. *Biorheology* 38, 335–345.
- Budday, S., Nay, R., de Rooij, R., Steinmann, P., Wyrobek, T., Ovaert, T.C., Kuhl, E., 2015. Mechanical properties of gray and white matter brain tissue by indentation. *J. Mech. Behav. Biomed. Mater.* 46, 318–330.
- Budday, S., Sommer, G., Birkl, C., Langkammer, C., Haybaeck, J., Kohnert, J., Bauer, M., Paulsen, F., Steinmann, P., Kuhl, E., Holzapfel, G.A., 2017a. Mechanical characterization of human brain tissue. *Acta Biomater.* 48, 319–340.
- Budday, S., Sommer, G., Haybaeck, J., Steinmann, P., Holzapfel, G.A., Kuhl, E., 2017b. Rheological characterization of human brain tissue. *Acta Biomater* doi:10.1016/j.actbio.2017.06.024.
- Christ, A.F., Franze, K., Gautier, H., Moshayedi, P., Fawcett, J., Franklin, R.J., Karadottir, R.T., Guck, J., 2010. Mechanical difference between white and gray matter in the rat cerebellum measured by scanning force microscopy. *J. Biomech.* 43, 2986–2992.
- Darvish, K., Crandall, J.R., 2001. Strain conditioning in the dynamic viscoelastic response of brain tissue. In: *Proceedings of the 2001 Bioengineering Conference*.
- de Rooij, R., Kuhl, E., 2016. Constitutive modeling of brain tissue: current perspectives. *Appl. Mech. Rev.* 68, 010801.
- Destrade, M., Gilchrist, M.D., Murphy, J.G., Rashid, B., Saccomandi, G., 2015. Extreme softness of brain matter in simple shear. *Int. J. Non-Linear Mech.* 75, 54–58.
- Donnelly, B., Medige, J., 1997. Shear properties of human brain tissue. *J. Biomech. Eng.* 119, 423–432.
- Fallenstein, G., Hulse, V.D., Melvin, J.W., 1969. Dynamic mechanical properties of human brain tissue. *J. Biomech.* 2, 217–226.
- Forte, A.E., Gentleman, S.M., Dini, D., 2016. On the characterization of the heterogeneous mechanical response of human brain tissue. *Biomech. Model. Mechanobiol* doi:10.1007/s10237-016-0860-8.
- Franceschini, G., Bigoni, D., Regitnig, P., Holzapfel, G.A., 2006. Brain tissue deforms similarly to filled elastomers and follows consolidation theory. *J. Mech. Phys. Solids* 54, 2592–2620.
- Fung, Y.C., 1993. *Biomechanics: Mechanical Properties of Living Tissues*. & Business Media Springer Science.
- Galford, J.E., McElhaney, J.H., 1970. A viscoelastic study of scalp, brain, and dura. *J. Biomech.* 3, 211–221.
- Goriely, A., Geers, M.G.D., Holzapfel, G.A., Jayamohan, J., Jerusalem, A., Sivaloganathan, S., Squier, W., van Dommelen, J.A.W., Waters, S., Kuhl, E., 2015. Mechanics of the brain: perspectives, challenges, and opportunities. *Biomech. Model. Mechanobiol.* 14, 931–965.
- Goriely, A., Weickenmeier, J., Kuhl, E., 2016. Stress singularities in swelling soft solids. *Phys. Rev. Lett.* 117, 138001.
- Jin, X., Zhu, F., Mao, H., Shen, M., Yang, K.H., 2013. A comprehensive experimental study on material properties of human brain tissue. *J. Biomech.* 46, 2795–2801.
- Labus, K.M., Puttlitz, C.M., 2016. Viscoelasticity of brain corpus callosum in biaxial tension. *J. Mech. Phys. Solids* 96, 591–604.
- Lang, G.E., Stewart, P.S., Vella, D., Waters, S.L., Goriely, A., 2014. Is the Donon effect sufficient to explain swelling in brain tissue slices. *J. R. Soc. Interface* 11, 20140123.
- McKee, C.T., Last, J.A., Russell, P., Murphy, C.J., 2011. Indentation versus tensile measurements of young's modulus for soft biological tissues. *Tissue Eng. Part B: Rev.* 17, 155–164.
- Mehrabian, A., Abousleiman, Y., 2011. General solutions to poroviscoelastic model of hydrocephalic human brain tissue. *J. Theor. Biol.* 291, 105–118.
- Mihai, L.A., Chin, L.K., Janmey, P.A., Goriely, A., 2015. A comparison of hyperelastic constitutive models applicable to brain and fat tissues. *J. R. Soc. Interface* 20150486.
- Mihai, L.A., Budday, S., Holzapfel, G.A., Kuhl, E., Goriely, A., 2017. A family of hyperelastic models for human brain tissue. *J. Mech. Phys. Solids* 106, 60–79.
- Miller, K., Chinzei, K., 1997. Constitutive modelling of brain tissue: experiment and theory. *J. Biomech.* 30, 1115–1121.
- Miller, K., Chinzei, K., 2002. Mechanical properties of brain tissue in tension. *J. Biomech.* 35, 483–490.
- Moran, R., Smith, J.H., Garcia, J.J., 2014. Fitted hyperelastic parameters for human brain tissue from reported tension, compression, and shear tests. *J. Biomech.* 47, 3762–3766.
- Ogden, R., 1972. Large deformation isotropic elasticity-on the correlation of theory and experiment for incompressible rubberlike solids. *Proc. R. Soc. Lond. A* 326, 565–584.
- Pogoda, K., Chin, L., Georges, P.C., Byfield, F.J., Bucki, R., Kim, R., Weaver, M., Wells, R.G., Marcinkiewicz, C., Janmey, P.A., 2014. Compression stiffening of brain and its effect on mechanosensing by glioma cells. *New J. Phys.* 16, 075002.
- Prange, M.T., Margulies, S.S., 2002. Regional, directional, and age-dependent properties of the brain undergoing large deformation. *J. Biomech. Eng.* 124, 244–252.
- Rashid, B., Destrade, M., Gilchrist, M.D., 2012. Mechanical characterization of brain tissue in compression at dynamic strain rates. *J. Mech. Behav. Biomed. Mater.* 10, 23–38.
- Rashid, B., Destrade, M., Gilchrist, M.D., 2013. Mechanical characterization of brain tissue in simple shear at dynamic strain rates. *J. Mech. Behav. Biomed. Mater.* 28, 71–85.
- Rashid, B., Destrade, M., Gilchrist, M.D., 2014. Mechanical characterization of brain tissue in tension at dynamic strain rates. *J. Mech. Behav. Biomed. Mater.* 33, 43–54.
- Reese, S., Govindjee, S., 1998. A theory of finite viscoelasticity and numerical aspects. *Int. J. Solids Struct.* 35, 3455–3482.
- Shuck, L., Advani, S., 1972. Rheological response of human brain tissue in shear. *J. Basic Eng.* 94, 905–911.
- Sidoroff, F., 1974. Nonlinear viscoelastic model with intermediate configuration. *J. De. Mec.* 13, 679–713.
- Simo, J., 1992. Algorithms for static and dynamic multiplicative plasticity that preserve the classical return mapping schemes of the infinitesimal theory. *Comput. Methods Appl. Mech. Eng.* 99, 61–112.
- Sommer, G., Eder, M., Kovacs, L., Pathak, H., Bonitz, L., Mueller, C., Regitnig, P., Holzapfel, G.A., 2013. Multiaxial mechanical properties and constitutive modeling of human adipose tissue: a basis for preoperative simulations in plastic and reconstructive surgery. *Acta Biomater.* 9, 9036–9048.
- Sommer, G., Schiefel, A.J., Andra, M., Sacherer, M., Viertler, C., Wolinski, H., Holzapfel, G.A., 2015. Biomechanical properties and microstructure of human ventricular myocardium. *Acta Biomater.* 24, 172–192.
- Tully, B., Ventikos, Y., 2011. Cerebral water transport using multiple-network poroelastic theory: application to normal pressure hydrocephalus. *J. Fluid Mech.* 667, 188–215.
- Van Dommelen, J., Van der Sande, T., Hrapko, M., Peters, G., 2010. Mechanical properties of brain tissue by indentation: interregional variation. *J. Mech. Behav. Biomed. Mater.* 3, 158–166.
- Weber, G., Anand, L., 1990. Finite deformation constitutive equations and a time integration procedure for isotropic, hyperelastic-viscoplastic solids. *Comput. Methods Appl. Mech. Eng.* 79, 173–202.
- Weickenmeier, J., de Rooij, R., Budday, S., Steinmann, P., Ovaert, T., Kuhl, E., 2016. Brain stiffness increases with myelin content. *Acta Biomater.* 42, 265–272.
- Weickenmeier, J., de Rooij, R., Budday, S., Ovaert, T., Kuhl, E., 2017. The mechanical importance of myelination in the central nervous system. *J. Mech. Behav. Biomed. Mater.* 15 (4) doi:10.1016/j.jmbbm.2017.04.017.
- Whittall, K.P., Mackay, A.L., Graeb, D.A., Nugent, R.A., Li, D.K., Paty, D.W., 1997. In vivo measurement of t2 distributions and water contents in normal human brain. *Magn. Reson. Med.* 37, 34–43.